TITLE

Precise Therapeutic Targeting of Distinct *NRXN1*$^{+/-}$ Mutations

AUTHORS

Michael B. Fernando[1,2,4,5], Yu Fan[3]*, Yanchun Zhang[3]*, Sarah Kammourh[3], Aleta N. Murphy[1,2,4], Sadaf Ghorbani[5,6], Ryan Onatzevitch[2], Adriana Pero[3], Christopher Padilla[3], Lei Cao[3], Sarah Williams[1-4], Gang Fang[3#], Paul A. Slesinger[2#] & Kristen J. Brennand[2-5#]

AFFILIATIONS

[1] Graduate School of Biomedical Science, Icahn School of Medicine at Mount Sinai, New York, NY 10029

[2] Nash Family Department of Neuroscience, Icahn School of Medicine at Mount Sinai, New York, NY 10029

[3]Department of Genetics and Genomics, Icahn School of Medicine at Mount Sinai, New York, NY 10029

[4]Friedman Brain Institute, Black Family Stem Cell Institute, Pamela Sklar Division of Psychiatric Genomics, Icahn School of Medicine at Mount Sinai, New York, NY 10029

[5] Department of Psychiatry, Yale School of Medicine, New Haven, CT, 06520

[6]Haukeland University Hospital, Bergen, Norway

*These authors contributed equally

[#]Correspondence: kristen.brennand@yale.edu, paul.slesinger@mssm.edu and gang.fang@mssm.edu

KEYWORDS

Human induced pluripotent stem cells; *NRXN1*; alternative splicing; glutamatergic neurons; GABAergic neurons; genomics; neuropsychiatric disorder; disease modeling; precision medicine

ABSTRACT

As genetic studies continue to identify risk loci that are significantly associated with risk for neuropsychiatric disease, a critical unanswered question is the extent to which diverse mutations --sometimes impacting the same gene-- will require common or individually tailored therapeutic strategies. Here we consider this in the context of rare, heterozygous, and non-recurrent copy number variants (2p16.3) linked to a variety of neuropsychiatric disorders that impact *NRXN1*, a pre-synaptic cell adhesion protein that serves as a critical synaptic organizer in the brain. Complex patterns of *NRXN1* alternative splicing are fundamental to establishing diverse neurocircuitry, vary between the cell types of the brain, and are differentially impacted by unique patient-specific (non-recurrent) deletions. Progress towards precision medicine may require restoring each person's *NRXN1* isoform repertoires in a cell-type-specific manner**.** Towards this, here we contrast the cell-type-specific impact of unique patient-specific mutations in *NRXN1* using human induced pluripotent stem cells. Perturbations in *NRXN1* splicing causally lead to divergent cell-type-specific synaptic outcomes: whereas *NRXN1*$^{+/-}$ deletions result in a decrease in synaptic activity throughout glutamatergic neuron maturation, there is an unexpected increase in synaptic activity in immature GABAergic neurons. Both glutamatergic and GABAergic synaptic deficits reflect independent loss-of-function (LOF) and gain-of-function (GOF) splicing defects. Towards clinical relevance, we show that treatment with β-estradiol increases *NRXN1* expression in glutamatergic neurons, while antisense oligonucleotides knockdown mutant isoform expression across both glutamatergic and GABAergic neurons. Direct or indirect manipulation of *NRXN1* splicing isoforms provides a promising therapeutic strategy for treating humans with 2p16.3 deletions.

MAIN

Neurexins are pre-synaptic cell adhesion proteins that act as a synaptic organizer (*1*). There are three neurexin genes (*NRXN1*, *NRXN2*, and *NRXN3*) in mammals and each is highly alternatively spliced to produce hundreds of isoforms, primarily categorized into long alpha and shorter beta isoforms (*2*). The complex alternative splicing of neurexins allows for widespread expansion of protein-protein interaction capabilities (*3*), providing the basis for neurexins to interact with diverse post-synaptic ligands to establish and maintain neurotransmission. *NRXN1α* splice variants are specific to brain regions (*4*) and between cell types (*5*), but the cell-type-specific functional impact of individual isoforms remains unclear. Although rare in the population, large copy number variations (deletions or duplications) at the *NRXN1* locus 2p16.3, particularly those deleting exonic regions are highly penetrant, pleiotropic, and are strongly associated with several

neuropsychiatric diseases, including schizophrenia (odds ratio 14.4(ref. *6*)), autism spectrum disorder (odds ratio 14.9 (ref. *7*)), epilepsy (odds ratio 9.91 (ref. *8*)), intellectual disability (odds ratio 7.47 (ref. *9*)) and Tourette's syndrome (odds ratio 20.3 (ref. *10*)). These exonic deletions in *NRXN1* are non-recurrent (that is, they vary in size and location), making it difficult to determine the molecular mechanisms underlying their diverse clinical symptoms (e.g., diagnosis, severity, prognosis, and age-of-onset). In rodent studies, gene knock outs (KO) of each *NRXN(1-3)* is sufficient to produce an array of excitatory and inhibitory synaptic phenotypes (*1*). However, heterozygous KO produce modest behavioral and physiological changes *in-vivo (11)*. By contrast, however, *in-vitro* studies of engineered heterozygous *NRXN1*$^{+/-}$ human neurons reveal robust changes in excitatory neurotransmission that are not observed in matched *NRXN1*$^{+/-}$ mouse neurons (*12, 13*). While these studies do not evaluate how *NRXN1*$^{+/-}$ impacts the complex alternative splicing of the gene or the non-recurrent nature of the deletions, they collectively suggest that neurexins possess unique human neurobiology, and therefore, the impact of the distinct patient-specific *NRXN1*$^{+/-}$ must be specifically evaluated in human models.

Human induced pluripotent stem cell (hiPSC)-derived neurons provide an ideal platform to study *NRXN1α* alternative splicing. Previously we established that hiPSC-derived forebrain cultures, comprised of a mixture of glutamatergic and GABAergic neurons with residual astroglia, recapitulate the diversity of *NRXN1α* alternative splicing observed in the human brain, cataloguing 123 high-confidence *NRXN1α* isoforms (*14*). Furthermore, using patient-derived *NRXN1*$^{+/-}$ hiPSCs with unique 5' or 3' deletions in the gene, we uncovered wide-scale reduction in wildtype *NRXN1α* isoform levels and, robust expression of dozens of novel isoforms from the 3' mutant allele (*14*). Overexpression of individual wildtype isoforms ameliorated reduced neuronal activity in patient-derived *NRXN1*$^{+/-}$ hiPSC-neurons in a genotype-dependent manner, whereas mutant isoform expression decreased neuronal activity levels in control hiPSC-neurons (*14*). We therefore hypothesized that 5' deletions of the promoter region represent classical loss-of-function (LOF), while robust expression of 3' specific novel mutant isoforms can confer a gain-of-function (GOF) effect that cannot be rescued by overexpression of wildtype isoforms. Although *NRXN1* splicing varies between the cell types of the brain, the impact of non-recurrent *NRXN1*$^{+/-}$ deletions on cell-type-specific splicing patterns and synaptic function remains untested.

Given the multifaceted role of *NRXN1* in excitatory and inhibitory synapses, the lack of mechanistic understanding of how aberrant splicing impacts neuronal physiology in a cell-type *and* genotype-dependent manner presents a significant challenge for therapeutic targeting. To discover the disease mechanisms that underpin *NRXN1*$^{+/-}$ deletions, we leverage advanced 2D

lineage conversion, and 3D organoid models to simultaneously compare excitatory and inhibitory neurons across 5' LOF and 3' GOF deletions. We identified points of phenotypic divergence across glutamatergic and GABAergic neurons, which were independently validated in isogenic experiments to establish causal relationships between aberrant splicing and synaptic dysfunction. Finally, we inform and test the design of novel therapeutic agents for *NRXN1*$^{+/-}$ deletions on LOF/GOF stratified patient mechanisms.

RESULTS

Shared aberrant splicing in patient-specific glutamatergic and GABAergic neurons.

To examine the impact of *NRXN1*$^{+/-}$ deletions in two different neuronal cell types, we used lineage conversion of patient hiPSCs for generating either excitatory glutamatergic neurons or inhibitory GABAergic neurons. Transient overexpression of *NGN2* in hiPSCs produces iGLUT neurons that are >95% pure glutamatergic neurons, robustly express glutamatergic genes, release glutamate, and produce spontaneous synaptic activity by day 21 in vitro (*15-18*). On the other hand, transient overexpression of *ASCL1* and *DLX2* yields iGABA neurons that are >80% positive for expressing GABA and GAD1/2 by day 35 in vitro, and possess mature physiologic properties of inhibitory neurons by day 42 (*16, 19*). We combined these highly efficient iGLUT and iGABA induction protocols with hiPSCs from patients with rare heterozygous intragenic deletions in *NRXN1* (*14*). Two cases containing the same ~136-kb deletion in the 3'-region of *NRXN1* (3' del) and two cases with ~115-kb deletions in the 5'-region of *NRXN1* (5'-Del). For controls, we used four passage-matched and sex-balanced subjects (**Fig. 1a,b**). Immunostaining confirmed expression of neurotransmitter transporters, vGLUT1 and vGAT for iGLUT and iGABA neurons, respectively (**Fig. 1c,h**). RNA-sequencing (RNAseq) further validated iGLUT (DIV21) and iGABA (DIV35) neuronal induction in all donors (**Fig. 1d,i**).

We first compared the transcriptomics of *NRXN1*$^{+/-}$ deletions with controls for both iGLUT and iGABA neurons. RNAseq analyses revealed overlap of the top differentially expressed genes (DEGs) across cell types/genotypes (e.g., *FAM66D, TTC34, GALNT9*), whereas the majority of case/control DEGs were genotype-specific (**Fig. 1e,j**). Gene-ontology analyses revealed a robust enrichment of developmental and synaptic terms for the 5'-Del iGLUT condition over all other conditions. Using publicly curated gene lists (*20, 21*), risk enrichments for schizophrenia, bipolar disorder, and autism spectrum disorder were most enriched in iGLUT neurons from 5'-Del cases

and iGABA neurons from 3'-Del cases (**Fig. 1f,k and Extended Data Fig. 2**). Baseline transcriptional comparisons therefore suggested the potential of strong phenotypes for 5'-Del iGLUT neurons. Despite cell-type-specific *NRXN1* isoform profiles reported in healthy brains (*5*) and neurons (*14*), aberrant *NRXN1* alpha/beta exon usages were shared between *NRXN1*$^{+/-}$ iGLUT and iGABA neurons (**Fig. 1g,l**), whereby alpha exon usage decreased for 5'-Del and increased for 3'-Del in both types of neurons. These observations with specific iGLUT and iGABA neurons parallel those from our previous study using hiPSC-derived forebrain neurons, which was a mixture of glutamatergic and GABAergic neurons with astroglia (*14*).

Patient-specific alterations in spontaneous neural activity occur without changes in passive and excitable membrane properties.

To evaluate the functional consequence of *NRXN1*$^{+/-}$ deletions on neuronal activity, we conducted a population-level analysis of spontaneous neuronal activity using a multi-electrode array (MEA) with 5'-Del, 3'-Del or control neurons co-cultured with primary mouse glial cells for six weeks to promote maturation. Interestingly, spontaneous network activity (weighted mean firing rate, wMFR) in *NRXN1*$^{+/-}$ iGLUT neurons was reduced by over 40% in two independent time points, at weeks post induction (WPI) 4 and 6 (**Fig. 2a-c,** 5'-Del p=0.0011; 3'-Del, p<0.0001, 1-way ANOVA, Dunnet's test). We next examined the passive membrane properties using whole-cell patch-clamp electrophysiology. The cell capacitance, membrane resistance and resting membrane potentials did not significantly differ between 5'- and 3'-Del cases and control iGLUT neurons (**Fig. 2d**). To examine the intrinsic excitability, we compared the input-output curve for induced firing and found no statistical difference in the maximal number of evoked action potentials (**Fig. 2e,** 2-way ANOVA, Dunnett's test). Furthermore, the voltage-dependent sodium and potassium current densities were similar between 5'-Del, 3'-Del and control iGLUT neurons (**Extended Data Fig. 3a**). Taken together, these results suggest that changes in passive or intrinsic excitability membrane properties cannot explain the reduced firing observed on MEAs for 5'-Del and 3'-Del in iGLUT neurons.

In parallel, we generated iGABA neurons with the same 5'-Del, 3'-Del, and control hiPSCs, as above. We observed that immature *NRXN1*$^{+/-}$ iGABA neurons exhibited a robust ~2-fold increase in population-wide wMFR activity (WPI2-3) from both 5'-Del and 3'-Del cases (5'-Del p=0.0381; 3'-Del, p=0.0047, 1-way ANOVA, Dunnet's test) (**Fig. 2f,g**). Though unexpected for GABA neurons, the finding is consistent with activation of ionotropic GABA receptors leading to depolarization due to little KCC2 expression and reduction of internal chloride levels (*22*). Indeed,

immature iGABA neurons expressed higher (10-fold increase compared to WPI2 neurons) levels of *SLC12A5* (the gene encoding *KCC2*) (**Extended Data Fig. 4a** p<0.0001, 2-way ANOVA, Dunnet's test). Furthermore, this transient hyperexcitability was pharmacologically inhibited by 10μM gabazine, a selective $GABA_A$ antagonist (**Extended Data Fig. 4b,c**). In mature iGABA neurons (>5 weeks), post-*KCC2* switch, the average wMFR decreased in 5'-Del and 3'-Del neurons (5'-Del p=0.0809; 1-way ANOVA, Dunnet's test) (**Fig. 2h**). Like iGLUT neurons, the passive and intrinsic excitability membrane properties of iGABA neurons were not different between *NRXN1*$^{+/-}$ 5'-Del or 3'-Del and controls (**Fig. 2i-j**, **Extended Data Fig. 3b**).

Overall, these data suggest that patient-specific changes in spontaneous neural activity are not driven by differences in passive and excitable membrane properties in iGLUT or iGABA neurons from *NRXN1*$^{+/-}$ 5'-Del and 3'-Del patients. Furthermore, these deletions did not appear to alter maturation of iGLUT or iGABA neurons, as evidenced by similar induced firing rates and resting membrane potentials.

NRXN1$^{+/-}$ 5' and 3' deletions result in divergent synaptic transmission deficits.

To further dissect the factors mediating phenotypes in altered spontaneous firing, we next investigated the efficacy of synaptic transmission in iGLUT and iGABA neurons. Voltage-clamp recordings of spontaneous excitatory post-synaptic currents (sEPSCs, no TTX) in iGLUT neurons revealed decreased frequency of events for both for 5'-Del and 3'-Del cases (**Fig. 3a**). The cumulative probabilities of inter-event-intervals (IEI) for both 3'-Del (P= 1.27E-11, Levene's test) and 5'-Del iGLUTs (5'-del P= 2.44E-5) (**Fig. 3a,b**) was significantly increased, compared to controls. The sEPSC amplitude increased for 5'-Del neurons (**Fig. 3a,c**). Miniature excitatory post-synaptic currents (mEPSCs, +TTX) showed similar trends in IEI but no changes in amplitude sizes across genotypes (IEI 5'-del P =0.0411, 1-way ANOVA, Dunnett's test) (**Extended Data Fig. 5a,b**). These reductions in synaptic transmission are consistent with the transcriptomic signatures; pre-synaptic (SynGO) genes showed a larger change (than post-synaptic) in synaptic gene expression signatures (5'-del Pre-SynGO, Log_2FC = 0.1252; 3'-del Pre-SynGO, Log_2FC= -0.0156) (**Fig. 3d,e**). We further probed transcriptional signatures of known *NRXN1* trans-synaptic interaction partners that mediate synapse formation, function, plasticity and are frequently linked with neuropsychiatric disease (*23*), and found they were represented in DEGs, including *CBLN2*, *LRRTM4* and *NXPH1*, suggesting these synaptic effects are largely driven by change in *NRXN1* expression (**Fig. 3f**).

By contrast, synaptic transmission in iGABA neurons appeared to be enhanced. The frequency of spontaneous inhibitory post-synaptic currents (sIPSCs) increased, marked by a significant decrease in IEI in 3'-Del iGABA neurons (3'-del P= 0.050E-5 by Levene's test) (**Fig. 3g-i)**. There was no change in sIPSC amplitude (**Fig. 3i**). Miniature inhibitory post-synaptic currents (mIPSCs) recorded in the presence of TTX and CNQX (AMPA/Kinate receptor antagonist) revealed similar trends in IEI, with no change in mIPSC amplitudes (**Extended Data Fig. 5c-d**). Similarly, SynGO analysis revealed concordant changes in synaptic transmission and transcriptomic signatures at 3'-del Pre-SynGO (Log_2FC = 0.0324), and represented of DEGs among *NRXN1* trans-synaptic interaction partners *CBLN2*, *NLGN1*, *NXPH1, CASK,* and *LRRTM2-4* (**Fig. 3j-l)**.

Overall, patient-specific alterations in spontaneous neural activity were driven by synaptic deficits, with the cell type-specific impact of aberrant *NRXN1* splicing resulting in divergent neurotransmission phenotypes. Furthermore, non-recurrent LOF and GOF presented unequal effect sizes between cell-types, with 5'-Del neurons being most impacted by excitatory transmission, but 3'-Del neurons being affected by both excitatory and inhibitory transmission. Given that deletions affected iGLUT and iGABA neurons in opposing directions, these findings may implicate *NRXN1* as a key mediator of excitatory/inhibitory balance, a prevalent theme among neuropsychiatric disorders (*24*).

Region-specific organoids resolve non-autonomous defects of neurogenesis and neuronal development.

To explore the impact of aberrant *NRXN1* splicing on neural patterning (*25*) within a self-organized microenvironment, we applied dorsal forebrain patterning to yield 5'-Del, 3'-Del and control human cortical organoids (hCOs) that resemble the pallium, or applied ventral forebrain patterning to generate human subpallial organoids (hSOs) that resemble the subpallium (**Fig. 4a,h**) (*26, 27*). Organoid sizes varied at early time points, but maintained consistency across genotypes by 4 months (**Extended Data Fig. 6a,b,g,h**). RT-qPCR validated dorsal and ventral patterning, and further confirmed robust expression of mutant isoforms exclusively from the 3'-Del patients, with no expression from 5'-Del and control organoids (**Extended Data Fig. 6c-e, i-k**). To unbiasedly characterize transcriptomics of cortical and subpallial organoids, we performed single cell RNA-seq (n = 47,460 cells from hCOs, n= 35,563 cells from hSOs using 10x genomics) at 6 months, a timepoint with well characterized neural activity (*26, 28*). We identified subclusters of cell-types within hCOs and hSOs (**Fig.4b,i**), and confirmed consistent distributions of cell clusters across genotypes (**Fig. 4c,j**). Strong expression of *NRXN1* and *FOXG1* confirmed

forebrain identity (and excluded one of six cell lines), while *EMX1* expression confirmed dorsalization of remaining hCOs. Likewise, *DLX2* expression confirmed ventralization of hSOs, with an enrichment of GABAergic-fated neurons (**Fig. 4d,k**).

A recent study demonstrated that KO of *NRXN1* increased replication of NPCs in human cells and in the *xenopus* telencephalon (*29*). To test if *NRXN1*$^{+/-}$ deletions could impact neurogenesis, we quantified neural rosette proliferation detected with immunofluorescence by calculating the ratio of *KI67* protein to *SOX2* protein expression, as markers of proliferative cells and multipotent neural stem cells. In the hCO subtype (DIV55-62), 3'-Del patient rosettes exhibited increased KI67:SOX2 compared to control (P= 0.0063, by 1-Way ANOVA) (**Fig. 4e-f**), while in the hSO subtype, 5'- and 3'-Del rosettes had reduced *KI67:SOX2* ratios (5'-del P= 0.0004; 3'-del P= 0.0004, by 1-Way ANOVA) (**Fig. 4l-m**). These results may explain the variation in NPC:neuron proportions across genotypes (**Fig. c,j**). Differentially expressed gene sets identified cell-type-specific effects in hCO-glutamatergic, hSO-GABAergic, and astroglia clusters, with robust enrichment of GO terms related to RNA splicing (from upregulated genes), and neurodevelopment and synaptic function (from downregulated genes) (**Fig. 4g,n**). Much of the enriched GO terms overlapped among hCO-glutamatergic and hSO-GABAergic neurons, and unexpectedly certain GO terms also reached significance in hCO-astroglia, but not hSO-astroglia clusters (**Extended Data Fig. 7**). Overall, these data suggest that patterns of divergent cell-type specific effects, particularly at the level of neural precursor states, persisted in our 3D models of forebrain development, resulting in significant changes to glutamatergic and GABAergic neurons.

Isogenic validation of divergent synaptic deficits, and therapeutic targeting of stratified patients.

To further support our findings of opposing, cell-type-specific changes in glutamatergic and GABAergic synaptic transmission, with unequal effect size between non-recurrent *NRXN1* deletions, we utilized a more direct approach using isogenic lines to causally link aberrant splicing to synaptic dysfunction and develop candidate therapies (**Fig. 5a,h**). First, we utilized short hairpin RNAs (shRNAs) to knockdown wildtype or mutant splice isoforms to mimic LOF or rescue GOF phenotypes, respectively. Targeted knockdown of constitutively expressed exon 9 (expressed in all alpha isoforms but not beta isoforms) achieved mRNA knockdown of ~55% in iGLUT neurons, and ~75% in iGABA neurons across two or more isogenic pairs (compared to a non-targeting control shRNA) (**Extended Data Fig. 8**). In iGLUT neurons, we observed decreased synaptic transmission (i.e., increased sEPSC IEI, P= 2.2E-16 by Levene's Test) (**Fig. 5b,c**), whereas in

iGABA neurons we observed increased synaptic transmission (decreased IEI, P = 2.2E-16 by Levene's Test and P= 0.0250 by 1-way ANOVA) (**Fig. 5d,e**), similar to the changes with 5'-Del neurons (**Fig. 3b,h**). Altogether, knockdown of wildtype splicing recapitulated cell-type-specific differences in *NRXN1*$^{+/-}$ 5'-Del neurons, causally implicating decreased wildtype *NRXN1*α expression (LOF) as a key driver of opposing cell-type-specific phenotypes.

To reverse the LOF, we pursued approaches that could enhance transcription of *NRXN1*α. β-estradiol was recently reported to reverse *NRXN1* LOF neurogenesis deficits in xenopus and human NPC models (*29*). Although the mechanism of rescue remains unknown, chromatin immunoprecipitation with sequencing (ChIP-Seq) in mouse brain tissue identified estrogen receptor alphaα (ERα) binding sites at the *NRXN1* alpha locus (**Extended Data Fig. 9**) (*30*). Consistent with *NRXN1* being a canonical target of ERα, acute treatment with β-estradiol (10nM or 30nM, 3-5 days) significantly increased *NRXN1*α expression in iGLUT neurons (P= 0.0297 by 1-way ANOVA) but not in iGABA neurons derived from 5'-Del (1 male, 1 female) and matched controls (1 male and 1 female) (**Fig. 5f**).

For *NRXN1 3*'-Del neurons, we reasoned that reducing the expression of the GOF transcript should restore the changes in synaptic transmission for both iGLUT and iGABA neurons. We designed a shRNA against the mutant splice junction overlapping exons 20 and 24, expressed in all 3'-Del unique *NRXN1* alpha and beta isoforms, and achieved targeted knockdown of mutant splice isoforms by 95% in iGLUT, and 25% in iGABA neurons in both donors (Extended Data Fig 6). In the donor with most robust knockdown in both iGLUT (90%) and iGABA (37%) neurons, electrophysiological recordings revealed reversal of changes in synaptic transmission. In iGLUT neurons, shRNA MT decreased sEPSC IEI (P= 3.66E-08 by Levene's Test and P= 0.0361) (**Fig. 5i,j**) and in iGABA neurons increased sIPSC IEI (P = 4.23E-02 by Levene's Test) (**Fig 5k,l**), as compared to shRNA-SCR. Notably, the IEIs for rescued neurons appeared similar to those for control iGLUT and iGABA neurons (**Fig. 3b,h**).

To investigate a more feasible therapeutic approach, we investigated the utility of anti-sense oligonucleotides (ASO), an appealing strategy for their recent clinical use to treat neurological diseases (*31*), on GOF 3'-Del patients. We designed an ASO that targets the mutant splice junction to facilitate a targeted RNAseH1 dependent degradation of mutant isoforms. Acute ASO treatment (1uM, 3-5 days) resulted in 50-60% knockdown of total mutant isoforms in iGLUT (P< 0.001 by student's t-test) and iGABA neurons (P= 0.0016 by student's t-test) relative to a non-targeting ASO (**Fig. 5g,n**). Altogether, increased *NRXN1* expression in 5'-Del neurons and

knockdown of mutant splicing in 3'-Del neurons can each rescue the opposing cell-type-specific case/control differences in *NRXN1*$^{+/-}$ neurons, implicating *NRXN1*α expression as a key a driver of *NRXN1* mutant phenotypes.

DISCUSSION

NRXN1$^{+/-}$ deletions are linked to diverse clinical outcomes, all of which have been associated with excitatory-inhibitory (E:I) imbalance[1,27,30]. Here, we show that *NRXN1* splicing bidirectionally regulates E:I synaptic transmission, with the 5'-Del and 3'-Del patients reducing sEPSCs but increasing sIPSCs in iGLUT and iGABA neurons, respectively. These changes likely play a critical role in altering the E:I balance, a common theme among neuropsychiatric disorders. Using a case/control *NRXN1*$^{+/-}$ cohort as well as isogenic manipulations of the *NRXN1* isoform repertoire, we report distinct phenotypic effects in human iGLUT and iGABA neurons, which predominately manifest in changes in the frequency of synaptic transmission. These results suggest causal relationships between aberrant splicing and synaptic dysfunction, dictated by unique patient-specific mechanisms. A recent report evaluated the impact of *NRXN1*$^{+/-}$ on forebrain organoids by single cell transcriptomic characterization over time, and highlighted specific perturbations in the developmental trajectories of early neural progenitors (*32*). Likewise, we report divergent proliferation dynamics, with an increase in glutamatergic enriched hCOs, but a decrease in GABAergic-enriched hSOs. While it is mechanistically unclear how mutations in *NRXN1* impact neurogenesis, prior evidence also exists for this phenomenon (*29, 33*), altogether suggesting roles for *NRXN1* beyond mediating synaptic organization and transmission, perhaps similar to *SYNGAP1* (*34*), a gene canonically thought to have exclusive synaptic function. Nevertheless, our causal demonstration of manipulating *NRXN1* splicing, which resulted in the recreation/rescue of synaptic phenotypes in post-mitotic neurons suggests that direct manipulation of splicing may achieve therapeutic benefit in cases.

Neurexins are expressed across all synapses and among certain non-neuronal cell-types, such as astrocytes, which may confer distinct functional roles (*35*). With respect to GOF mechanisms, it remains unclear whether mutant isoforms shift the stoichiometry of alternative splicing against wildtype RNA isoforms or alter trans-synaptic protein-protein interactions. Unique patterns of aberrant splicing amongst non-recurrent mutations would be challenging to target with a common pharmacological agent for all *NRXN1*$^{+/-}$ carriers. Given that *NRXN1* fundamentally encodes for pre-synaptic cell adhesion molecules, traditional neuropharmacological agents that target specific receptors within single neurotransmission systems would be unlikely to broadly ameliorate the

311 many levels of neural circuitry impacted across neurodevelopment. Instead, precision therapies
312 that target aberrant splicing are needed to effectively reverse defects in the multiple cell types
313 affected by patient-specific deletions.

314 Our results show that the opposing effects of *NRXN1*$^{+/-}$ in glutamate and GABA neurons provides
315 the foundation for evaluating proof-of-concept therapeutics that target aberrant splicing, once the
316 LOF or GOF phenotype has been determined. We find that ASOs designed to target the mutant
317 splice junction and facilitate degradation of mutant isoforms provides a therapeutic approach to
318 ameliorate the toxic effects of GOF mutations. While gene therapy in brain disease has resulted
319 in mixed successes (*36*), cases of muscular dystrophies which have been treated via splicing
320 modulating ASOs have proved effective (*37*). For LOF mutations, mechanisms for upregulating
321 wild-type allele are needed. Applying steroid-based pharmaceuticals for treating LOF mutations
322 is also feasible, as they have been used to treat neuroinflammation-related conditions (*38*), with
323 recent studies revealing estrogen-mediated roles in neuroprotection (*29*), demonstrating the
324 safety and feasibility of this approach. Altogether, precision medicine provides therapeutic
325 promise for treating neuropsychiatric conditions.

326 Our findings with estrogen-dependent regulation of *NRXN1* expression also hint at possible
327 mechanistic explanations for the dramatic sex differences in the prevalence and severity of autism
328 spectrum disorders, for which the biological basis for the prominent male bias in diagnosis is
329 unknown (*39*). At the genetic level, evidence exists for a female protective effect – the observation
330 that females have a higher threshold for reaching affectation status and require greater mutational
331 burden to express ASD phenotypes due to female-specific protective factors that lead to
332 resilience (*40, 41*). Estradiol ameliorates neurodevelopmental phenotypes in *Xenopus* and
333 zebrafish genetic models of ASD (*29, 42*), suggesting that estradiol might be modulating relevant
334 circuits in the setting of ASD risk genes to mitigate a range of ASD gene mutations. Estradiol
335 modulates excitatory and inhibitory circuits in the developing brain, regulating the switch from
336 excitatory to inhibitory GABAergic signaling in the hippocampus and playing a neuroprotective
337 role against glutamate-induced excitotoxicity (*43, 44*). Consistent with our findings with *NRXN1* in
338 human neurons, estrogens may modulate neurodevelopment at the cellular and circuit levels,
339 conferring resilience in ASDs.

340 While our work carefully considers the cell-type specific impact of *NRXN1* splicing on non-
341 recurrent deletions, it is important to acknowledge certain limitations inherent in our study.
342 Notably, the neuronal subtypes that are yielded from lineage conversion can be diverse and

immature, as recently characterized (*45*). Furthermore, the impact of *NRXN1*$^{+/-}$ on synaptic physiology across different subtypes of neurons (e.g., SST versus PV expressing GABA neurons), remains to be determined. Future studies will need to comprehensively assess the impact of *NRXN1*$^{+/-}$ across more discrete cell types and complex multicellular systems. Furthermore, it will be important to also probe the biochemical and proteomic interactions of *NRXN1*. Unbiased proximity-labelling methods such as BioID (*46*), could provide mechanistic insights into *NRXN1* medicated synapse function, by defining alternations in binding profiles from wildtype and mutant isoforms.

Based on our strategy of manipulating splicing as a therapeutic strategy for specific *NRXN1* mutations, a similar approach could be applied to loss- and gain-of-function mechanisms linked to mutations in other neuropsychiatric disorder-related synaptic genes (e.g., *NLGN3* (*47*), *CACNA1D* (*48*), *CACNA1C (49), SCN2A* (*50*)). Taken together, our work highlights important implications for precision medicine treatments of neuropsychiatric disorders, demonstrating the necessity of functionally dissecting the phenotypic impact of diverse patient-specific genetic variants across cellular contexts, to resolve candidate therapies across stratified disease mechanisms.

METHODS

Plasmid designs and molecular cloning

i. TetO-Ascl1-Neo

The *ASCL1* insert from TetO-Ascl1-Puro (Addgene #97329) was synthesized as a gBLOCK flanked by EcoR1 cut sites, and cloned into TetO-hNgn2-Neo using EcoR1 to remove *NGN2.* The recipient vector was dephosphorylated with shrimp alkaline phosphatase (rSAP NEB #M0371S) during the digest, column purified and ligated at a 1:1 vector to insert ratio using the QuickLig Kit (NEB #M2200S). The *ASCL1* stop codon was subsequently mutated using the QuickChange II-XL site-directed mutagenesis kit (Agilent #200523) and verified via whole plasmid sequencing from plasmidsaurus.

ii. shRNA RNA interference constructs

All shRNAs were designed and produced by Sigma-Aldrich via custom submitted sequences

against wildtype *NRXN1α* (constitutively expressed exon 9) and mutant *NRXN1α* (mutant 20/24 splice junction) cloned into TCR2 pLKO.5-puro.

Cell Culture

i. hiPSC culture

Passage matched (±3) human induced pluripotent stem cells (hiPSCs) were cultured in StemFlex media (Life technologies #A3349401) on Matrigel (Corning, #354230). At ~70-80% hiPSCs were clump passaged using 0.5mM EDTA in PBS without Mg/Ca (Life technologies #10010-031). Cells were washed once and incubated for 4-7 min with EDTA at RT. The EDTA was aspirated, and the remaining colonies were lifted off with 1mL of StemFlex and re-distributed at varying densities in a 6–well maintenance plate. hiPSC lines were split every 4-6 days. For neuronal/organoid differentiation, wells of similar confluence across all hiPSC donors were resuspended and seeded onto a Matrigel coated 10cm dish and expanded until ~70-80% confluency.

ii. HEK293T culture and lenti-viral production

HEK293T cells were maintained in 15cm dishes and cultured in DMEM supplemented with 10% standard FBS (Life technologies #16000069). 3rd Gen lenti-viral particles were produced using previously described methods and REV, MDL and VSV-G plasmid ratios (Man-Ho et al., 2015), each transfected with PEImax (Polysciences #24765-1). Each PEIMax batch was volumetrically titrated at total ugDNA:uLPEI for optimal transfection efficiency.

iii. Primary mouse glia production

All mouse work was performed under approved IACUC protocols at the Icahn School of Medicine at Mount Sinai. C57BL/6 mice were used as breeding pairs. For glial preps, dissected cortices from 3 pups (at p0-3) were dissociated using papain (R&D #LS003126) and plated on 10cm dishes in MEF medium (DMEM, 10% Cosmic Calf Serum (Fisher #SH3008703HI), 1x Antibiotic-antimycotic (Life technologies #15240), 1x Sodium Pyruvate (Life technologies #11360070), 1x MEM Non-Essential Amino Acids Solution (Life technologies #11140050), 4uL 2-Mercaptoethanol (Sigma #60-24-2), supplemented with 100µg/mL Normocin (InvivoGen #ant-nr-2). Glial cells were recovered and propagated for 7 days, expanded into three 10cm dishes and were used for co-culture experiments. All glial preps were tested twice for mycoplasma (Normocin withdrawn) (Lonza, #LT07-318) prior to freezing or neuronal co-culture. At day 14, one 10cm dish with mouse glia were distributed to two MEA, 12- or 24- well plates, and subsequently inactivated with 4µM

Ara-C (Sigma #C1768) prior to or during re-seeding of induced neurons.

iv. iGLUT induction and astrocyte co-culture

At day -1 hiPSCs expanded in 10cm dishes were dissociated with accutase (StemCell Technologies, #07920), washed and pelleted with a 1:4 ratio of accutase to DMEM for 5 min at 1000 rcf, and re-suspended with StemFlex media containing ROCK inhibitor, THX (10μM/mL; Sigma Aldrich, SML1045). The hiPSCs are then co-transduced with TetO-Ngn2-Puro (Addgene #79049) or TetO-Ngn2-Neo (Addgene# 99378) and UCb-rtTA (legacy vector from the lab of Fred Gage) and seeded at 1.0-1.5x10^6 cells in 1.5mL per well on 6-well plates were coated with 2x Matrigel for at least one hour at 37C. The hiPSC-viral mixture was then incubated overnight. The following morning (day 0), a full media change with iGLUT induction media was performed with the following recipe: Neurobasal Media: 1x N2 (Life technologies #17502-048), 1x B-27 minus Vitamin A (Life technologies #12587-010), 1x Antibiotic-Antimycotic, 1x Sodium Pyruvate, 1x GlutaMax (Life technologies #35050), 500μg/mL cyclic-AMP (Sigma #D0627), 200nM L-ascorbic acid (Sigma #A0278), 20ng/ml BDNF (Peprotech #450-02), 20ng/ml GDNF (Peprotech #450-10), 1μg/ml natural mouse laminin (Life technologies #23017015). On days 1-2, iGLUT cells were treated with respective antibiotic concentrations at 1ug/mL puromycin (Sigma# P7255) or 0.5ug/mL neomycin (Life technologies #11811-031). On day 3, antibiotic medium was withdrawn and iGLUT cells were treated with 4μM Ara-C. On Day 4, iGLUT cells were dissociated with accutase for 15 min, washed and pelleted with a 1:4 ratio of accutase to DMEM for 5 min at 800 rcf, and re-suspended with iGLUT media containing ROCK inhibitor, Ara-C and 2% low-hemoglobin FBS (R&D systems #S11510). iGLUT neurons were distributed among wells (500-750k cells per 24wp or 0.75-1.5E6 cell per 12wp) pre-seeded with confluent mouse glia. The following day, iGLUT neurons received a full media change with Brainphys maturation media (Neurobasal Media, 1x N2, 1x B-27 minus Vitamin A, 1x Antibiotic-Antimycotic, 500μg/mL cyclic-AMP, 200nM Ascorbic Acid, 20ng/ml BDNF, 20ng/ml GDNF, 2% low-hemoglobin FBS, 1μg/ml Mouse Laminin) supplemented with Ara-C and were subsequently monitored for growth of non-neuronal/glial cells. Ara-C treatment was tittered down with half-media changes (without Ara-C) every 3-4 days until used for experiments.

v. iGABA induction and astrocyte co-culture

iGABA production paralleled the methods aforementioned. hiPSCs were instead co-transduced with TetO-Ascl1-puro (Addgene #97330) or TetO-Ascl1-neo (Addgene #TBD), TetO-Dlx2-hygro

(Addgene #97329) and UCb-rtTA and seeded at 0.8-1.2x10^6 cells in 1.5mL per well on 6-well plates similarly prepared. The following morning (day 0), a full media change with iGABA induction media (DMEM/F-12 + Glutamax, 1x N2, 1x B-27 minus Vitamin A, 1x Antibiotic-Antimycotic) was performed. On days 1-2 iGABA cells were selected with respective antibiotic concentrations at 1µg/mL puromycin or 0.5ug/mL neomycin and 0.25ug/mL hygromycin (Life Technologies #10687010), followed by antibiotic withdrawal and Ara-C treatment on day 3. iGABA neurons were re-seeded identically to iGLUT cells, at 150-250k cells per 24wp well. iGABA cultures were morphologically QC'ed prior to all experiments, with uncharacteristic batches being discarded.

vi. Cortical and subpallial organoid differentiation

Cortical organoids were generated according to the protocol described by Sloan et. al. (*51*), with several modifications. hiPSCs were first aggregated into embryoid bodies (EBs) using an AggreWell™800 Microwell Culture Plate system (Stemcell Tech #34850). Expanded hiPSCs were rinsed twice with DPBS without Ca/Mg, and then dissociated using accutase. 3x10E6 hiPSCs were added to a single well in the prepared AggreWell and allowed to aggregate in a 37 °C incubator for 24 hours. The following day (day 0), EBs were dislodged from the AggreWell plate using a cut p1000 pipette tip and passed over a 40µm strainer, and washed with excess DMEM. The strainer was inverted over an Ultra-Low Attachment 10 cm culture dish and the EBs were collected in spheroid induction media, which contained Stemflex supplemented with two SMAD inhibitors, SB-431542 (SB) and LDN193189 (LDN), and THX. The following day (day 1), the media THX was withdrawn. From d2-d6, induction media was replaced daily, and no longer contained the Stemflex supplement (only base Stemflex media with SB and LDN). On day 6, the media was replaced with organoid patterning media, formulated with Neurobasal-A medium, 1x B-27 minus Vitamin A, 1x GlutaMAX, and 1x Antibiotic-Antimycotic. From d6-d24, organoid maturation media was supplemented with 20 ng/ml of EGF (R&D Systems, #236-EG) and 20 ng/ml FGF2 (R&D Systems, #233-FB-01M). Media was changed every day from d6 – d15, after which media was changed every other day. From d25-d43, the organoid maturation media was supplemented with 20 ng/ml of NT-3 (PeproTech, #450-03) and 20 ng/ml BDNF. From d43 onwards, organoids received organoid maturation media with no supplements, and media was changed every 4 days or as needed. Subpallial organoids were generated in the same way as cortical organoids, but with additions in media formulations. From d4-d23, hSOs received spheroid induction media or organoid maturation media supplemented with 5 µM of the Wnt inhibitor, IWP-2 (Selleckchem, #S7085). From d12-d23, hSO organoids received neuronal differentiation media supplemented with 100 nM of the SHH agonist, SAG (Selleckchem,

#S7779).

Electrophysiology

i. Multi-electrode array (MEA)

The Axion Maestro (Middleman) system was used to perform all MEA recordings. Measurements began as early as DIV9 for both iGLUT and iGABA co-cultures. For time course experiments, MEA plates were recorded every 2-3 days per week with a full media change prior to each recording.

ii. Whole-cell patch-clamp electrophysiology

For whole-cell patch-clamp recordings, iGLUT or iGABA human-mouse glia co-cultures were recorded at 4-6 weeks following dox-induction (time points specified in figure legends), with a full media change one day prior to recording. Cells were visualized on a Nikon inverted microscope equipped with fluorescence and Hoffman optics. Neurons were recorded with an Axopatch 200B amplifier (Molecular Devices), digitized at 10 kHz using a Digidata 1320a (Molecular Devices) and filtered between 1-10 kHz, using Clampex 10 software (Molecular Devices). Patch pipettes were pulled from borosilicate glass electrodes (Warner Instruments) to a final tip resistance of 3-5 MΩ using a vertical gravity puller (Narishige). Neurons were recorded in Brainphys medium (external solution) with an internal patch solution containing (in mM): K-d-gluconate, 140; NaCl, 4; MgCl2, 2; EGTA, 1.1; HEPES, 5; Na2ATP, 2; sodium creatine phosphate, 5; Na3GTP, 0.6, at a pH of 7.4. Osmolarity was 290-295 mOsm. Neurons were chosen at random using DIC and all recordings were made at room temperature (~22°C). Current-clamp measurement occurred across -10pA to +50pA steps, with a maximum stimulus of +60pA, whereas voltage-clamp measurements occurred across -50mV to +50mV steps, normalized to cell capacitance (to control for variable neuronal size). For sEPSC/sIPSC recordings, the internal solution was replaced with (in mM): Cesium-Chloride, 135; HEPES-CoOH, 10; QX-314, 5; EGTA, 5. Osmolarity was 290-295 mOsm. All mEPSC measurements were recorded under the presence of 100nM TTX-citrate (Tocris Cat# 1069). mIPSC measurements were made using 100nM TTX-citrate and CNQX-disodium salt (Tocris Cat#1045/1) to pharmacologically inhibit ionotropic glutamate receptors. All chemicals were purchased from Sigma-Aldrich Co. (St. Louis, MO). All toxic compounds were handled in accordance with ISMMS EHS standards.

iii. Patch-clamp data analysis

All patch-clamp data were analyzed on Clampfit (v) and Easy-Electrophysiology (v2.4.1 or beta-versions). Briefly, for voltage-clamp data, files were opened in Easy-Electrophysiology and two bins were assigned for Na+/K+ measures for minimum and maximum current values, respectively. For current-clamp data, files were opened in Easy-Electrophysiology and action potential (AP) analysis was used to automatically determine spike number and properties. For gap-free recordings, all data was post-hoc adjusted to a baseline of zero on ClampFit, and subsequently analyzed in Easy-Electrophysiology by template and linear threshold detection. For case control experiments, a minimum cutoff of 10 events for the duration of the recording (3min) was used as QC. For typical EPSC events, a single template from a randomly chosen recording was used to analyze all traces (with a 30ms decay cutoff). For IPSC events, three templates were used to detect variable GABA receptor kinetics, for all traces (with a 60ms decay cutoff). An amplitude cut off of 7pA was used to call positive events. For cumulative probabilities, each cell was binned by experiment and averaged across all cells for a representative curve (GraphPad Prism v).

RNA-Sequencing and bioinformatic analyses

i. Bulk RNA sequencing and DEG analysis of iGLUT and iGABA neurons

iGLUT (DIV21) and iGABA (DIV14 or DIV35) co-cultured with primary mouse glia (to match functional experiments) were harvested in Trizol and submitted to the New York Genome Center (*52*) for high-throughput RNA extraction and quality control, library prep using the Kapa Hyper library prep with ribo-erase (Roche #KK8541) and subsequently sequenced on Illumina NovaSeq. Returned raw data files were first processed to remove mouse reads in the RNA-seq data, a combined genome reference (hg38 and mm10) was created using the "mkref" command in cellranger v6.1.2. The raw sequencing reads were then aligned to the combined genome reference using STAR v2.7.2a (*53*). Reads that mapped specifically to the human reference genome were extracted from the resulting BAM files for subsequent gene expression analysis. Gene-level read counts were obtained using the Subread v2.0.1 package featureCount (*54*), and RPKM values were calculated using the R package edgeR (*55*). To confirm sample identity, variants were called from RNA-seq bam files by HaplotypeCaller and GenotypeGVCFs in GATK v4.2.0.0. Then bcftools v1.15 was used to examine variants concordance with variants from whole-exome sequencing data from the same donor. Following donor identity confirmation, the differential gene expression analysis followed the methods as described previously (*56*). First, CibersortX (*57*) was utilized to predict differences in cell type composition across all samples. The R package variancePartition v1.30.2 (*58*) was then employed to investigate the contribution of

specific variables to the variance in gene expression. The limma/voom package (*59*) was used for differential expression analysis, with the regression of fibroblast and hiPSC cell type compositions. The analysis began with a comparison between the case and control groups. Subsequently, within each case vs control group, subgroup comparisons were conducted for all four pairs (two donors each for 3'-Del and 5-Del patients and two healthy controls) of samples, accounting for heterogeneity between different donors. Genes with a fold change larger than 1.5 between the patient and control group, an FDR less than 0.1, and a fold change larger than 1.5 in all four pairs of subgroup comparisons were defined as the final set of differentially expressed genes. Kallisto v0.46.1 (*60*) was used to calculate the *NRXN1* exon usage ratios.

ii. Network Analysis of top DEGs overlapping with disease risk genes

The ASD, BP, and SCZ risk gene lists were extracted from previously curated gene lists (*20*), Genes with the top 200 smallest FDR values and a fold change larger than 1.5 in the case vs control comparison were selected for the protein interaction network analysis. Then, overlapping genes between the selected gene list, the disease risk gene sets, and the proteins in the SIGNOR database (*21*) were utilized to query the SIGNOR database and build the interaction network, using the "connect + add bridge proteins" search mode in The SIGNOR Cytoscape App v1.2. (*61*)

iii. Dissociation and 10x Single-Cell RNA sequencing of organoids

Whole organoids were dissociated to the single cell level in preparation for single-cell RNA sequencing using the Papain Worthington Kit (Worthington, LK003150). All solutions included in the kit were prepared according to the manufacturer's instructions. 4-6 organoids were transferred to one well of a low attachment 6 well plate and were washed with PBS without Ca^{2+} and Mg^{2+}. Organoids were cut with a small scalpel into smaller pieces for easier dissociation. 800 µl of papain solution (supplied in the kit) was added per well. Samples were incubated at 37°C for about two hours or until single cell suspension was achieved. Every 15 minutes, the mixture was pipetted up and down with a cut P1000 pipette tip. Once single cell suspension was reached, 500 µl of inhibitor solution (supplied in the kit) was added to the well. The solution was gently mixed, filtered through a 70 µm-pore sieve, and transferred to a 15 ml centrifuge tube. The cells were pelleted by centrifugation at 300 x g for 5 minutes at room temperature. Cell pellets were resuspended in 500 µl of ice-cold 0.04% BSA diluted in PBS without Ca^{2+} and Mg^{2+}. scRNA-seq was performed on 4-6 pooled 6-month-old organoids per donor line, per condition (hCS or hSS) for a total of 48 organoids. A minimum of 10,000 dissociated cells were submitted for sequencing.

The library was prepared using the Chromium platform (10x Genomics) with the 3' gene expression (3' GEX) V3/V3.1 kit. Libraries were sequenced on an Illumina NovaSeq sequencer with an S4 flow cell, targeting a minimum depth of 20,000 reads per cell. The lengths for read parameters Read 1, i7 index, i5 index, and Read 2 were 100, 8, 0, 100, respectively.

iv. Bioinformatic analysis of scRNASeq data

The raw sequencing data, represented as base call (BCL) files produced by the Illumina sequencing platform, were subjected to demultiplexing and subsequent conversion into FASTQ format using CellRanger software (version 6.0.0, 10x Genomics) with default parameters. The software then mapped the FASTQ reads to the human reference genome (GRCh38) with default parameters. Following this, the 'count' command in the Cell Ranger v6.0.0 software was utilized for the quantification of gene expression. For alignment and counting, the reference genome refdata-gex-GRCh38-2020-A was used, which was procured from the official 10x Genomics website. We performed QC and normalization using the Seurat v3 R package (*62*). For QC, we filtered out low-quality cells using the following criteria: (i) cells with unique gene counts outside the range of 200 to 6000; (ii) cells with more than 30% mitochondrial gene content; and (*63*) cells with less than 2000 unique molecular identifiers (*64*). Post QC, we carried out normalization, scaling the gene expression measurements for each cell by the total expression, multiplied by a scale factor (10,000 by default), and log-transformed the results. We extracted the expression profiles of the 338 genes identified by Birrey et al (*26*), to reduce the dimensionality of the dataset through principal component analysis (PCA), and identify statistically significant PCs using a JackStraw permutation test. This was followed by non-linear dimensional reduction using the UMAP (Uniform Manifold Approximation and Projection) technique for visualization. Cells were clustered based on their PCA scores using the Shared Nearest Neighbor (SNN) modularity optimization-based clustering algorithm in Seurat. After dimensionality reduction, we used known marker genes to guide the clustering of cells. Each cluster was then annotated using cell type markers identified by Birey et al (*26*). Finally, we conducted differential expression analysis across the defined cell clusters using the FindAllMarkers function in Seurat, which employs a Wilcoxon Rank-Sum test. The significantly differentially expressed genes were then used to interpret the biological significance of cell clusters. For each identified cell type, we conducted an enrichment analysis using the WebGestalt (WEB-based GEne SeT AnaLysis Toolkit) online tool, with the Human genome (GRCh38) as the reference set, employing a hypergeometric statistical method and the Benjamini & Hochberg method for multiple test adjustment.

v. Analysis of ChIP-sequencing data from β-estradiol treated rodent brains.

Tracks in bigWig format were downloaded from the GEO dataset GSE144718 (*30*). Two peaks within the *NRXN1* gene region in the mm10 genome were visualized using Spark v2.6.2 (*65*)

Therapeutic Treatments of iNeurons

i. Beta-Estradiol treatment

Beta-Estradiol was reconstituted in DMSO and subsequently diluted in Brainphys maturation media for a final concentration of 10 or 30nM. Neurons were treated for 3-5 consecutive days, with fresh drug or vehicle control replenished daily. iGLUT and iGABA neurons were treated starting from ~DIV14-18. On the final day of treatment, cells were harvested ~4 hours post dosage.

ii. Antisense Oligonucleotide treatment

A single HPLC-grade ASO was designed from Qiagen (LNA GapmeR) against the mutant (Ex 20/24) splice junction containing a phosphorothioate modified backbone with or without a 5'-FAM label for fluorescent visualization. All experiments were performed matched with a non-targeting ASO as the control group. ASOs were delivered using Lipofectamine RNAiMAX Transfection Reagent (Thermo, #13778075). The Lipofectamine RNAiMAX was diluted in Opti-MEM Medium (Thermo, #31985070). ASO was then diluted in Opti-MEM Medium. The diluted ASO was added in a 1:1 ratio to the diluted Lipofectamine RNAiMAX and incubated at room temperature for 5 minutes. The ASO-lipid complex was added to cells, and incubated for 72 hours post-transfection, until RNA harvest.

Molecular Biology and Imaging

i. RNA extraction and RT-qPCR

For the isolation of RNA, 2D cells were lysed using TRIzol (Life Technologies #15596026) and purified using the Qiagen miRNeasy Kit (Qiagen Cat# 74106) according to the manufacturer's instructions. For 3D organoids, pooled (early timepoints) or single organoids were washed and lysed using TRIzol, by manual homogenization with a pestle in a 1.5mL centrifuge tube. Following purification, samples were normalized within each experiment (15-50ng) and subsequently used

for RT-qPCR assays using the *Power* SYBR Green RNA-to-Ct 1-Step Kit (Thermo REF 4389986). Relative transcript abundance was determined using the ΔΔCT method and normalized to the *ACTB* housekeeping gene. All primer sequences are listed below.

shRNA, primers and oligonucleotide probe sequences

Target	Sequences (5'-3')	Supplier
RT-qPCR Primer Probes		
NRXN1 (wildtype) Forward	AGAAAGATGCCAAGCACCCA	ThermoFisher
NRXN1 (wildtype) Reverse	CCCATGTCCAGGAGGAGGTA	ThermoFisher
NRXN1-20/24 (mutant) Forward	GCTACCCTGCAGCCAACC	ThermoFisher
NRXN1-20/24 (mutant) Reverse	GACCATACCCGTGGTGCTG	ThermoFisher
ACTB Forward	TGTCCCCCAACTTGAGATGT	ThermoFisher
ACTB Reverse	TGTGCACTTTTATTCAACTGGTC	ThermoFisher
MAP2 Forward	AAACTGCTCTTCCGCTCAGACACC	ThermoFisher
MAP2 Reverse	GTTCACTTGGGCAGGTCTCCACAA	ThermoFisher
NEUROD1 Forward	GGTGCCTTGCTATTCTAAGACGC	ThermoFisher
NEUROD1 Reverse	GCAAAGCGTCTGAACGAAGGAG	ThermoFisher
SLC17A7 Forward	CGCATCATGTCCACCACCAACGT	ThermoFisher
SLC17A7 Reverse	GAGTAGCCGACCACCAACAGCAG	ThermoFisher
SLC17A6 Forward	TCAACAACAGCACCATCCACCGC	ThermoFisher
SLC17A6 Reverse	GTTTCCGGGTCCCAGTTGAATTTGG	ThermoFisher
GAD65 Forward	CTATGACACTGGAGACAAGGC	ThermoFisher

GAD65 Reverse	CAAACATTTATCAACATGCGCTTC	ThermoFisher
DLX5 Forward	ACAGAGACTTCACGACTCCCAG	ThermoFisher
DLX5 Reverse	TGTGGGGCTGCTCTGGTCTA	ThermoFisher
shRNA Sequences		
NRXN1 wildtype mRNA (Exon 9)	ATGGAGTGGTGGCATTTAAAT	Sigma
NRXN1 mutant mRNA (Overlapping Exon 20/24)	CGCTACCCTGCAGCCAACCCA	Sigma
Antisense Oligonucleotides (LNA Gapmers)		
Non-targeting ASO	AACACGTCTATACGC/36-FAM/	Qiagen
NRXN1-Splice ASO	GGTTGGCTGCAGGGTA/36-FAM/	Qiagen

ii. Bright Field Imaging

For organoid perimeter analyses, brightfield microscope images of organoids were taken with a 2x objective. Image analysis was performed in ImageJ, with best fitting ovals or ellipses were selected around an organoid, and perimeter was measured.

iii. Immunostaining of 2D cultures

For immunostaining of 2D monocultures, iGLUT and iGABA neurons seeded on acid-etched coverslips coated with PEI buffered with boric acid and 4x Matrigel. Samples were washed with DPBS $Ca^{2+/}Mg2^{+}$ and fixed using cold, fresh 16% paraformaldehyde (Life Technologies, #28908), diluted to 4% for 12 minutes at RT. Coverslips were then blocked and permeabilized with 2% donkey serum in DPBS $Ca^{2+/}Mg2^{+}$ supplemented with 0.1% Triton-X (Sigma, #93443-100ML) (blocking buffer), for one hour at RT. Primary antibody solutions were prepared in blocking buffer and incubated overnight at 4°C. The following day, samples were washed three times with PBS, and treated with secondary antibodies diluted in blocking buffer, for 1 hour in a dark chamber. Finally, samples were washed three times, and stained with DAPI for 15min at RT during the final wash. Coverslips were mounted with antifade (Vectashield #H-1000-10) onto glass slides and

stored at 4°C until imaging using an upright Zeiss LSM 780 confocal microscope.

iv. Immunostaining 3D cultures

For immunostaining of 3D organoids, samples were first washed with DPBS $Ca^{2+}/Mg2^{+}$ and fixed using cold 4% PFA for 2 hours at 4°C. Organoids were then washed with DPBS $Ca^{2+}/Mg2^{+}$ supplemented with 10% sucrose (Sigma, #S0389-500G) for one hour. Sucrose percent was increased to 20% for an additional hour, and finally 30% for an overnight incubation. The following day, upon observing the organoids saturated sunk to the bottom of the 1.5mL tube, organoids were transferred to OCT (Sakura #4583) twice in order to remove residual sucrose solution, and snap frozen in a cryopreservation mold with dry ice and stored at –80°C until cryosectioned. Organoids were sectioned at 20 µm thickness onto a Superfrost *Plus* slide (Fisher Scientific, #22-037-246) and stored at -20°C until immunohistochemistry staining. Boundaries were drawn around tissue sections with a lipid pen (Fisher Scientific, #NC9545623) to contain solution and slides were washed once with DPBS with Ca^{2+}/Mg^{2+} to remove excess OCT compound. Slides were then washed twice with 0.01% Triton-X in DPBS with Ca^{2+}/Mg^{2+} (DPBS-TX) and were blocked in 2% Donkey Serum in DPBS-TX for one hour at RT. Primary antibody incubation mixtures were diluted in 2% Donkey Serum in DPBS-TX (see below for a list of primary and secondary antibodies and dilutions used). 100 µl of primary antibody mixtures was added per slide, and allowed to incubate overnight in a humidified chamber at 4°C. Pieces of parafilm were added on top of primary antibody mixtures to further prevent dehydration of slides. The following day, slides were washed three times with DPBS-TX. Secondary antibodies were diluted in DPBS-TX and were allowed to incubate for an hour. Slides were again washed three times with DPBS-TX. A 1:2000 DAPI solution diluted in DPBS-TX was applied to slides for 10 minutes. Secondary and DAPI stainings took place in a covered chamber in order to minimize exposure to light. Slides were washed twice with DPBS-TX, and then once with DPBS with Ca^{2+} and Mg^{2+}. Slides were mounted with coverslips using Aqua Polymount solution (Polysciences #18606-20). Slides were stored at -20 °C until they were imaged.

Target	Antibody Dilution	Supplier/ CAT#
<u>Primary Antibodies</u>		
MAP2AB	1:500	Sigma, #M1406
(Rabbit) vGAT	1:500	Synaptic Systems, #135-303

(Rabbit) vGLUT1	1:500	Synaptic Systems, #131-002
SOX2	1:200	Santa Cruz Biotechnology, #sc-365964
(Rabbit) KI67	1:300	Abcam, #ab15580
(Chicken) MAP2	1:250	Aves Labs, #MAP
DAPI	1:1000	Sigma, #D9542
Secondary Antibodies		
(Donkey) 488-Mouse	1:200	Jackson ImmunoResearch, # 711-545-152
(Donkey) 568-Rabbit	1:200	Abcam, #ab175700
(Donkey) 647-Chicken	1:200	Jackson ImmunoResearch, # 703-605-155
(Donkey) 568-Mouse	1:500	Invitrogen (A10037)
(Donkey) 488-Rabbit	1:1000	Life Technologies (A-21206)

667

668

669 **Data and Code Availability**

670 All source donor hiPSCs have been deposited at the Rutgers University Cell and DNA Repository
671 (study 160; http://www.nimhstemcells.org/) and all bulk and single-cell transcriptome sequencing
672 data are being prepared for deposits to GEO. To facilitate improved reproducibility of our data
673 analyses, custom scripts will be deposited to github post peer-review.

674 **Acknowledgements**

675 MBF is supported by a Gilliam Fellowship from the Howard Hughes Medical Institute. This work
676 is supported by the National Institute of Mental Health grants RO1 MH121074-02 (KJB, GF and
677 PAS) and RO1 MH125579-02 (GF and KJB). We thank the Stem Cell Engineering Core at the
678 Icahn School of Medicine at Mount Sinai. The authors are grateful to the labs of Nan Yang (Ruiqi
679 Hu and Xiaoting Zhou) and Samuele Marro (Madel Durens) for assistance in primary glial

680 preparations. The authors thank Kayla G. Townsley and Mark G. Baxter for advice on statistical
681 testing. Finally, the authors thank all members of the Brennand, Slesinger and Fang labs for
682 critical feedback and discussions throughout the course of this work.

683 **Author Information**

684 MBF, SK, ANM, RO, CP, AP performed and analyzed experiments supervised by PAS and KJB.
685 YZ and YF performed bioinformatic analyses supervised by GF. SG contributed to RNASeq
686 analyses. SW produced virus for the generation of iGABA neurons. MBF, GF, PAS and KJB wrote
687 the paper with input from all authors.

688 **Ethics declarations / Competing interest statement.**

689 The authors have no competing interests to declare.

690

691 **Figures**

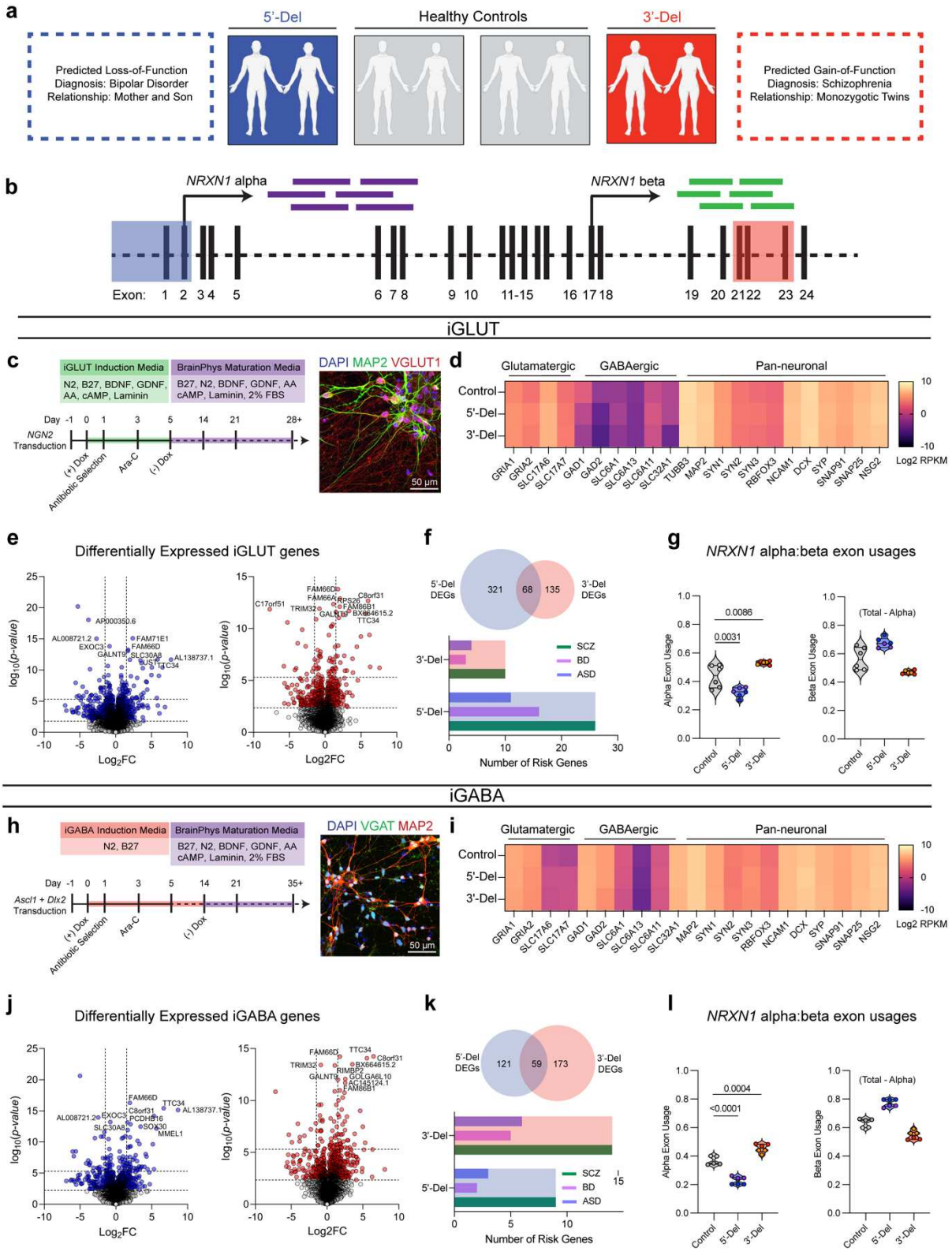

692

Figure 1. *Changes in NRXN1 splicing are conserved across human iPSC derived glutamatergic (iGLUT) and GABAergic (iGABA) neurons.* (a) Brief description of clinical information of all hiPSC lines used in this study, and (b) schematic of *NRXN1* gene structure with red and blue shades corresponding on 3'-Del and 5'-Del genotypes, respectively. Arrows indicate relative internal promoter positions with purple bars corresponding to alpha exons, and green bars correlating to beta exons. (c, h) Induction timeline and factors to generate iGLUT and iGABA neurons, with immunostaining validation of neuronal identity (MAP2), glutamate identity (vGLUT1), and GABA identity (vGAT). (d, i). Gene expression panel confirming abundance of neuronal markers and neurotransmitter identity (n = 6 donors | 2-3 RNASeq replicates per donor averaged within genotypes). (e, j) Volcano plots of differential gene expression (DE) analysis across both genotypes. Vertical dashed lines represent DE genes above/below 1.5 Log_2FC. Horizontal dashed lines represent FDR = 0.1 cutoff (lower) and Bonferroni corrected cutoff. (f, j) Overlap of DEGs between genotypes and enrichment of genes across neuropsychiatric disorders. (g) Percent usage of alpha *NRXN1* exon usage, compared via a 1-way ANOVA, with Dunnett's test, and (l) beta *NRXN1* exon usage, calculated by subtracting alpha-specific reads against total reads.

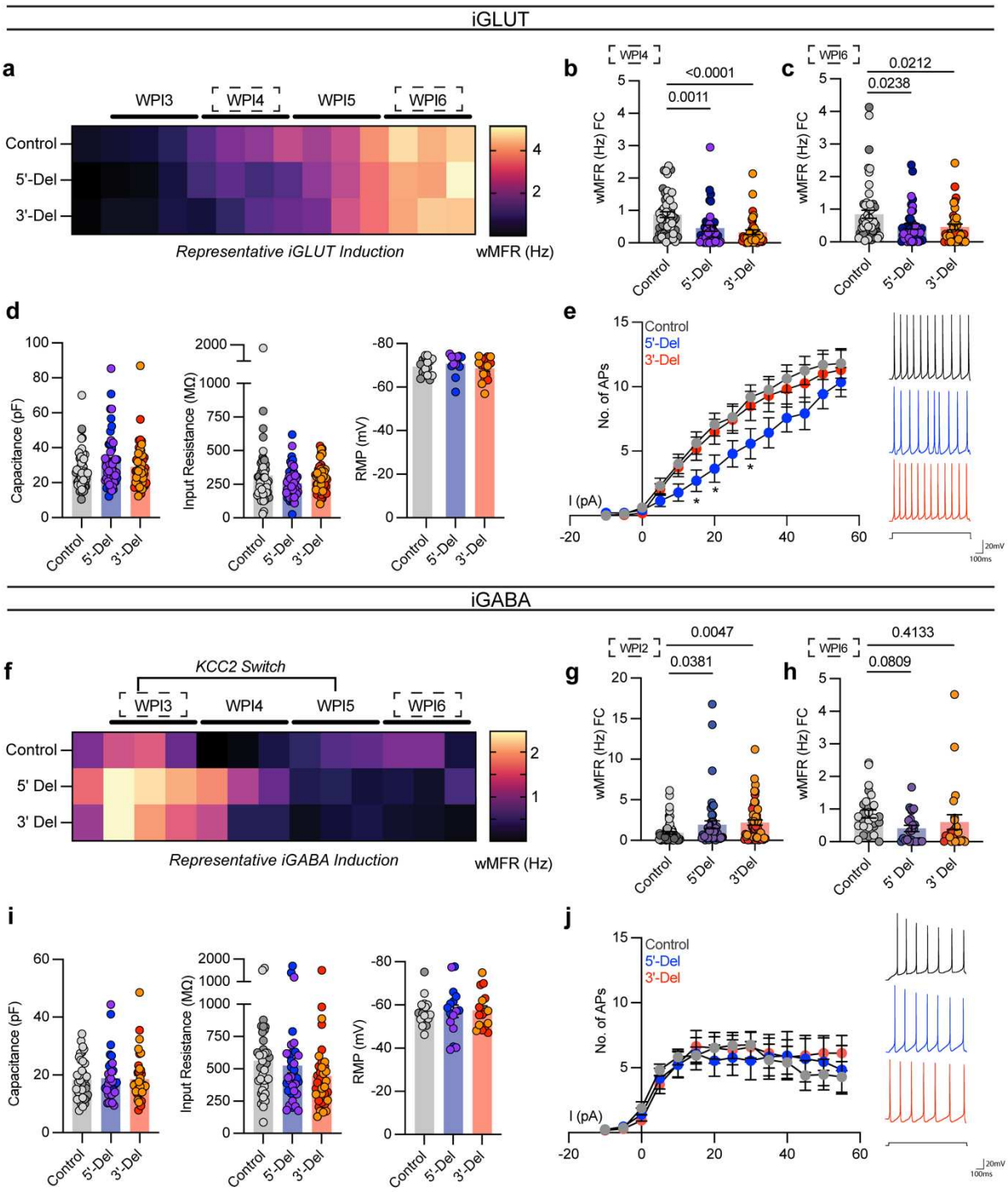

Figure 2. *Spontaneous, passive, and excitable membrane properties are minimally changed in NRXN1$^{+/-}$ induced neurons.* (a, f) Timelapse of multi-electrode array recordings every 2-3 days apart starting near ~DIV12 for a single representative induction. Tiles represent averaged wMFR values across genotypes during a single recording session. (b,c) Quantification of iGLUT neuronal

activity at WPI4 and WPI6; n= 6 donors | 3 inductions | 132 MEA wells. (g, h) iGABA activity at WPI2 (n = 8 donors | 5 inductions | 174 MEA wells), and WPI6 (n= 6 donors | 2 inductions | 73 MEA wells). (d) Passive measures of iGLUT membrane properties: cell capacitance (cm), input resistance (n = 6 donors | 2 inductions | 150 neurons), and membrane resistance (n = 6 donors | 2 inductions | 46 neurons). All p-values = n.s. via 1-way ANOVA, with Dunnett's test. (e) Input-output curves of excitable properties (n = 6 donors | 2 inductions | 36 neurons), with representative traces (right). Genotype effect p-val = n.s. via 2-Way ANOVA, with Dunnett's test. (i) Passive measures of iGABA membrane properties: cell capacitance (cm), input resistance (n = 6 donors | 2 inductions | 110 neurons), and membrane resistance (n = 6 donors | 2 inductions | 50 neurons). All p-values = n.s. via 1-way ANOVA, with Dunnett's test. (j) Input-output curves of excitable properties (n = 6 donors | 3 inductions | 47 neurons), with representative traces (right). Genotype effect p-val = n.s. via 2-Way ANOVA, with Dunnett's test.

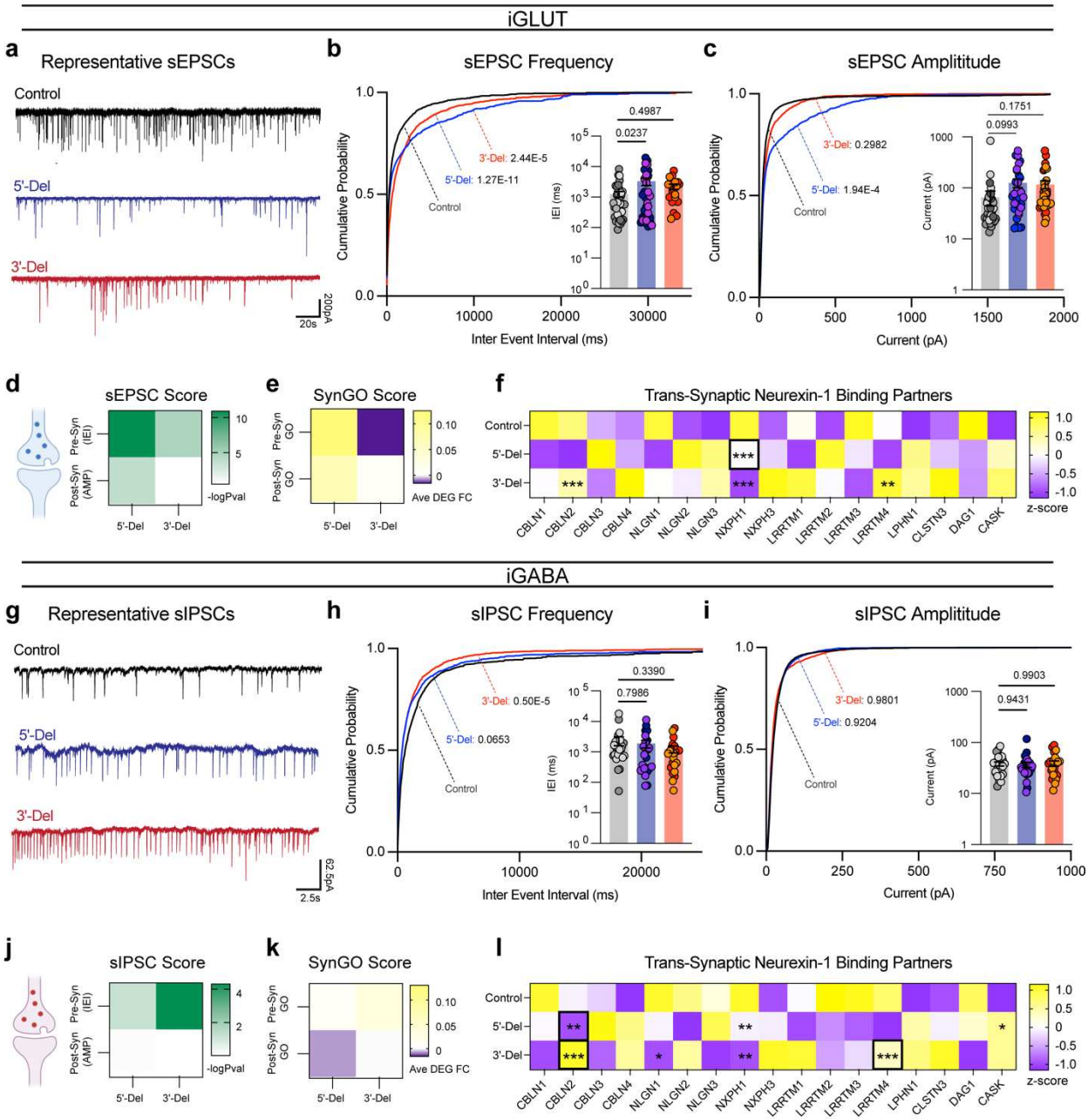

Figure 3: *Divergent impact of NRXN1$^{+/-}$ deletions on neurotransmission in induced neurons.* (a, e) Representative traces of sEPSCs and sIPSCs. (b, h), Cumulative probabilities of inter-event-internals (IEI), across genotypes (Compared by Levene's Test). Inset represent log-scaled IEI (compared by 1-way ANOVA, with Dunnett's test. (c, i), Cumulative probabilities of event amplitudes across genotypes (Compared by Levene's Test). Inset represent log-scaled amplitude (compared by 1-way ANOVA, with Dunnett's test); iGLUT n = 8 donors | 6 inductions | 91 neurons, iGABA n = 6 donors | 4 inductions | 73 neurons. (d, j) Transformed p-values of Levene's Test and

(e, k) SynGO gene-set averaged log_2FC values across pre- or post- synaptic genes. (f, l) Gene expression panel (RPKM fold change, relative to control donors), of canonical *NRXN1* binding partners, boxes indicate reaching genome wide significance. $*P < 0.05$, $**P < 0.01$, $***P < 0.001$, Wilcoxon's rank sum test, FDR = 0.05.

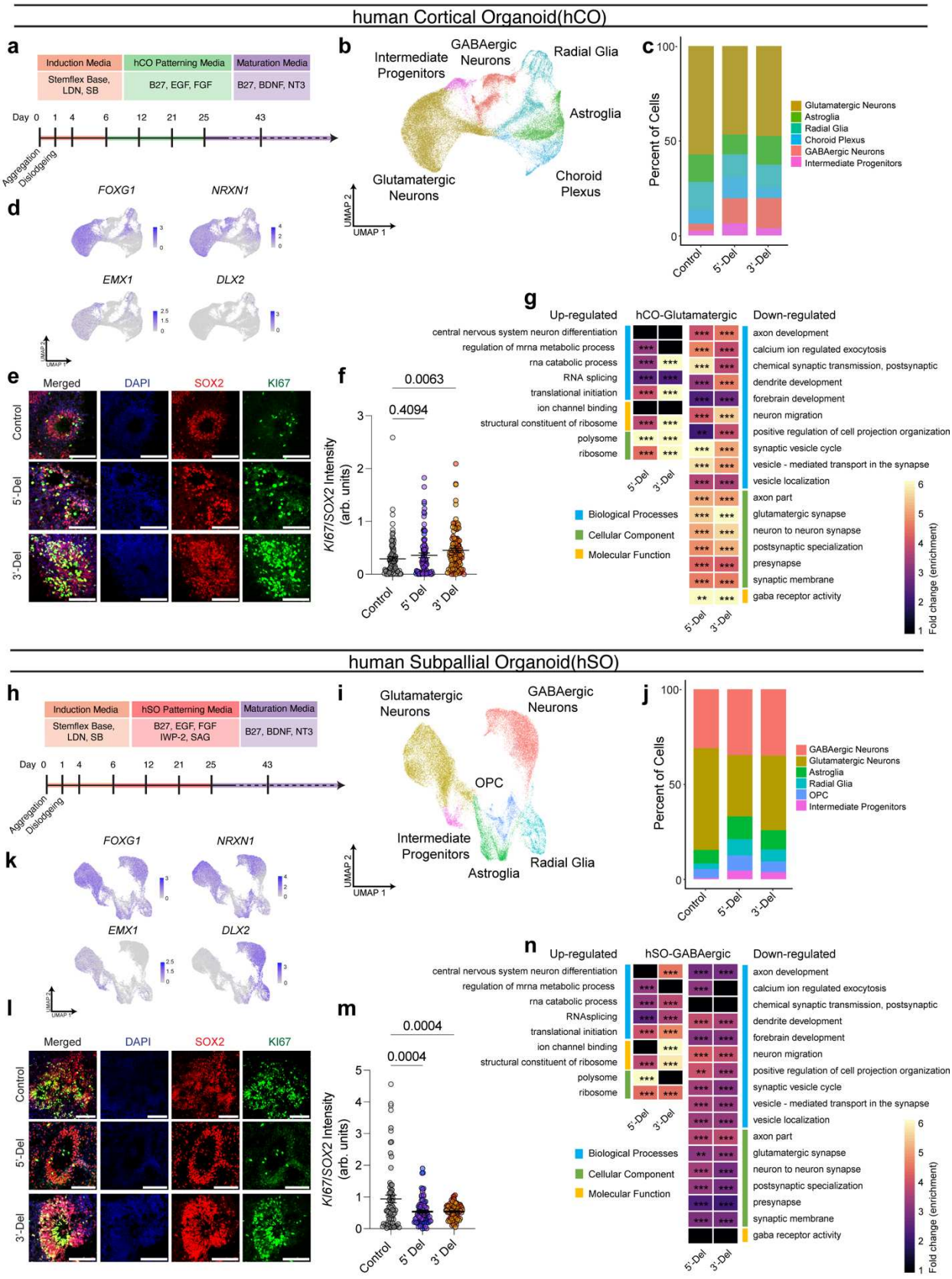

Figure 4: *NRXN1$^{+/-}$ deletions impact patterning of region-specific human brain organogenesis.* (a, h) Timeline of organogenesis protocols (b, i), UMAPs of human cortical organoid and subpallial organoid (hSO) samples sequenced at 6 months, annotated by cell clusters, and (c, j) relative proportions of cell clusters across genotypes, (hCO = 5 donors | 1 batch | 47,460 cells) and (hSO = 5 donors | 1 batch | 35,563 cells). (d, k) validation of regionalization across forebrain (*FOXG1*), dorsal (*EMX1*) and ventral (*DLX2*) regions, with *NRXN1* expression across all cells. (e, l) Representative images of neural rosettes, immunostained with SOX2, KI67 and DAPI, across genotypes with (f, m) quantified intensity ratios for hCO (n = 6 donors | 2 batches | 284 rosettes from 12 organoids) and hSO (n = 6 donors | 2 batches | 231 rosettes from 10 organoids), compared via 1-way ANOVA, with Dunnett's test. (g, n) Gene ontological analysis results using DEGs from scRNASeq. *P < 0.05, **P < 0.01, ***P <0.001, Wilcoxon's rank sum test, FDR = 0.05.

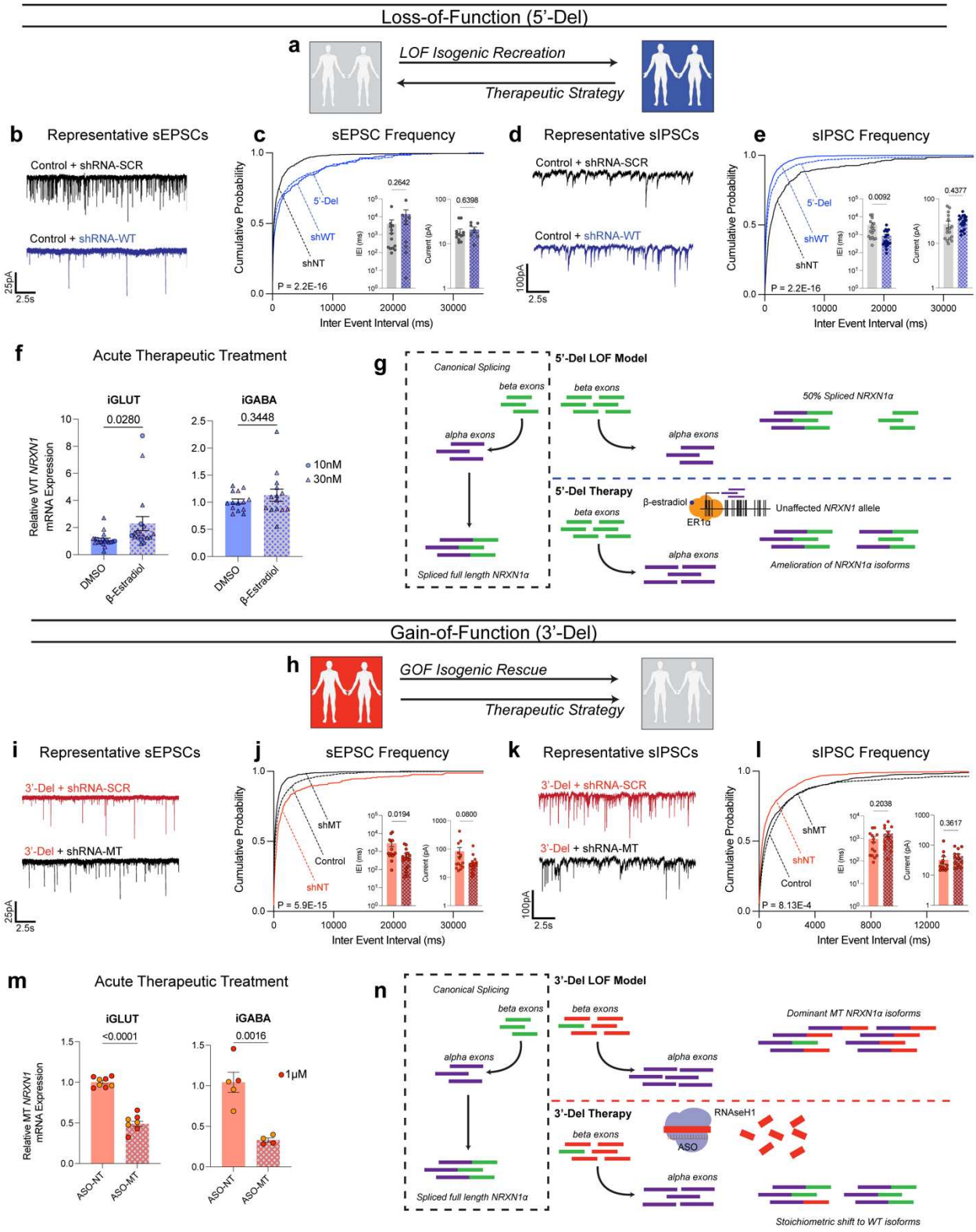

Figure 5: *Isogenic recapitulation and rescue of neurotransmission phenotypes, with strategies for precise therapeutic targeting.* (a, h) Schematic of isogenic and therapeutic strategies

(phenotypic recreation or rescue). (b) Representative traces of iGLUT wildtype knockdown effects, with (c) cumulative probabilities of sEPSC kinetics (insets represent log-scaled IEI and amplitude measures). Curves were compared via a Levene's test, and insets were compared via a 1-way ANOVA with Dunnett's test (iGLUT n = 1 isogenic pair | 2 inductions | 19 neurons). (d) Representative traces of iGABA wildtype knockdown effects, with (e) cumulative probabilities of sIPSC kinetics (insets represent log-scaled IEI and amplitude measures). Curves were compared via a Levene's test, and insets were compared via a 1-way ANOVA with Dunnett's test (iGABA n = 3 isogenic pairs | 2 inductions | 35 neurons). (f) Precision β-estradiol treatment of stratified LOF-patients (compared via a student's t-test). (g) Proposed 5'-Del LOF model and mechanism of action. (i) Representative traces of iGLUT mutant knockdown effects, with (j) cumulative probabilities of sEPSC kinetics (insets represent log-scaled IEI and amplitude measures). Curves were compared via a Levene's test, and insets were compared via a 1-way ANOVA with Dunnett's test (iGLUT n = 1 isogenic pair | 2 inductions | 32 neurons). (k) Representative traces of iGABA mutant knockdown effects, with (l) cumulative probabilities of sIPSC kinetics (insets represent log-scaled IEI and amplitude measures). Curves were compared via a Levene's test, and insets were compared via a 1-way ANOVA with Dunnett's test (iGABA n = 1 isogenic pairs | 2 inductions | 27 neurons). (m) Precision ASO treatment of stratified GOF-patients (compared via a student's t-test). (n) Proposed 3'-Del GOF model and mechanism of action.

References

1. T. C. Sudhof, Synaptic Neurexin Complexes: A Molecular Code for the Logic of Neural Circuits. *Cell* **171**, 745-769 (2017).
2. J. de Wit, A. Ghosh, Specification of synaptic connectivity by cell surface interactions. *Nat Rev Neurosci* **17**, 22-35 (2016).
3. X. Yang *et al.*, Widespread Expansion of Protein Interaction Capabilities by Alternative Splicing. *Cell* **164**, 805-817 (2016).
4. D. Schreiner *et al.*, Targeted combinatorial alternative splicing generates brain region-specific repertoires of neurexins. *Neuron* **84**, 386-398 (2014).
5. M. V. Fuccillo *et al.*, Single-Cell mRNA Profiling Reveals Cell-Type-Specific Expression of Neurexin Isoforms. *Neuron* **87**, 326-340 (2015).
6. C. R. Marshall *et al.*, Contribution of copy number variants to schizophrenia from a genome-wide study of 41,321 subjects. *Nat Genet* **49**, 27-35 (2017).
7. N. Matsunami *et al.*, Identification of rare recurrent copy number variants in high-risk autism families and their prevalence in a large ASD population. *PLoS One* **8**, e52239 (2013).
8. R. S. Moller *et al.*, Exon-disrupting deletions of NRXN1 in idiopathic generalized epilepsy. *Epilepsia* **54**, 256-264 (2013).
9. M. S. Ching *et al.*, Deletions of NRXN1 (neurexin-1) predispose to a wide spectrum of developmental disorders. *Am J Med Genet B Neuropsychiatr Genet* **153B**, 937-947 (2010).
10. A. Y. Huang *et al.*, Rare Copy Number Variants in NRXN1 and CNTN6 Increase Risk for Tourette Syndrome. *Neuron* **94**, 1101-1111 e1107 (2017).
11. H. M. Grayton, M. Missler, D. A. Collier, C. Fernandes, Altered social behaviours in neurexin 1alpha knockout mice resemble core symptoms in neurodevelopmental disorders. *PLoS One* **8**, e67114 (2013).
12. C. Pak *et al.*, Human Neuropsychiatric Disease Modeling using Conditional Deletion Reveals Synaptic Transmission Defects Caused by Heterozygous Mutations in NRXN1. *Cell stem cell* **17**, 316-328 (2015).
13. C. Pak *et al.*, Cross-platform validation of neurotransmitter release impairments in schizophrenia patient-derived NRXN1-mutant neurons. *Proc Natl Acad Sci U S A* **118**, (2021).

14. E. Flaherty *et al.*, Neuronal impact of patient-specific aberrant NRXN1alpha splicing. *Nat Genet* **51**, 1679-1690 (2019).
15. S. M. Ho *et al.*, Rapid Ngn2-induction of excitatory neurons from hiPSC-derived neural progenitor cells. *Methods* **101**, 113-124 (2016).
16. N. Barretto *et al.*, ASCL1- and DLX2-induced GABAergic neurons from hiPSC-derived NPCs. *J Neurosci Methods* **334**, 108548 (2020).
17. Y. Zhang *et al.*, Rapid single-step induction of functional neurons from human pluripotent stem cells. *Neuron* **78**, 785-798 (2013).
18. N. Schrode *et al.*, Synergistic effects of common schizophrenia risk variants. *Nat Genet* **51**, 1475-1485 (2019).
19. N. Yang *et al.*, Generation of pure GABAergic neurons by transcription factor programming. *Nat Methods*, (2017).
20. C. Seah *et al.*, Modeling gene x environment interactions in PTSD using human neurons reveals diagnosis-specific glucocorticoid-induced gene expression. *Nat Neurosci* **25**, 1434-1445 (2022).
21. P. Lo Surdo *et al.*, SIGNOR 3.0, the SIGnaling network open resource 3.0: 2022 update. *Nucleic Acids Res* **51**, D631-d637 (2023).
22. M. A. Virtanen, P. Uvarov, M. Mavrovic, J. C. Poncer, K. Kaila, The Multifaceted Roles of KCC2 in Cortical Development. *Trends in neurosciences* **44**, 378-392 (2021).
23. A. M. Gomez, L. Traunmüller, P. Scheiffele, Neurexins: molecular codes for shaping neuronal synapses. *Nature Reviews Neuroscience* **22**, 137-151 (2021).
24. V. S. Sohal, J. L. R. Rubenstein, Excitation-inhibition balance as a framework for investigating mechanisms in neuropsychiatric disorders. *Mol Psychiatry* **24**, 1248-1257 (2019).
25. S. T. Schafer *et al.*, Pathological priming causes developmental gene network heterochronicity in autistic subject-derived neurons. *Nat Neurosci* **22**, 243-255 (2019).
26. F. Birey *et al.*, Assembly of functionally integrated human forebrain spheroids. *Nature* **545**, 54-59 (2017).
27. S. J. Yoon *et al.*, Reliability of human cortical organoid generation. *Nat Methods* **16**, 75-78 (2019).
28. T. A. Khan *et al.*, Neuronal defects in a human cellular model of 22q11.2 deletion syndrome. *Nat Med* **26**, 1888-1898 (2020).
29. H. R. Willsey *et al.*, Parallel in vivo analysis of large-effect autism genes implicates cortical neurogenesis and estrogen in risk and resilience. *Neuron* **109**, 1409 (2021).

30. B. Gegenhuber, M. V. Wu, R. Bronstein, J. Tollkuhn, Gene regulation by gonadal hormone receptors underlies brain sex differences. *Nature* **606**, 153-159 (2022).
31. T. C. Roberts, R. Langer, M. J. A. Wood, Advances in oligonucleotide drug delivery. *Nature Reviews Drug Discovery* **19**, 673-694 (2020).
32. R. Sebastian *et al.*, Schizophrenia-associated NRXN1 deletions induce developmental-timing- and cell-type-specific vulnerabilities in human brain organoids. *Nature Communications* **14**, 3770 (2023).
33. L. Zeng *et al.*, Functional impacts of NRXN1 knockdown on neurodevelopment in stem cell models. *PLoS One* **8**, e59685 (2013).
34. M. Birtele *et al.*, The autism-associated gene SYNGAP1 regulates human cortical neurogenesis. *bioRxiv*, 2022.2005.2010.491244 (2022).
35. J. H. Trotter *et al.*, Astrocytic Neurexin-1 Orchestrates Functional Synapse Assembly. *BioRxiv*, (2020).
36. S. Ingusci, G. Verlengia, M. Soukupova, S. Zucchini, M. Simonato, Gene Therapy Tools for Brain Diseases. *Frontiers in pharmacology* **10**, (2019).
37. J.-B. Brunet de Courssou, A. Durr, D. Adams, J.-C. Corvol, L.-L. Mariani, Antisense therapies in neurological diseases. *Brain* **145**, 816-831 (2022).
38. C. Yilmaz *et al.*, Neurosteroids as regulators of neuroinflammation. *Frontiers in Neuroendocrinology* **55**, 100788 (2019).
39. E. National Academies of Sciences, Medicine, *Sex Differences in Brain Disorders: Emerging Transcriptomic Evidence: Proceedings of a Workshop*. L. Bain, S. M. P. Norris, C. Stroud, Eds., (The National Academies Press, Washington, DC, 2021), pp. 62.
40. A. Jack *et al.*, A neurogenetic analysis of female autism. *Brain* **144**, 1911-1926 (2021).
41. D. M. Werling, The role of sex-differential biology in risk for autism spectrum disorder. *Biol Sex Differ* **7**, 58 (2016).
42. E. J. Hoffman *et al.*, Estrogens Suppress a Behavioral Phenotype in Zebrafish Mutants of the Autism Risk Gene, CNTNAP2. *Neuron* **89**, 725-733 (2016).
43. M. M. McCarthy, Estradiol and the developing brain. *Physiol Rev* **88**, 91-124 (2008).
44. C. S. Woolley, Acute Effects of Estrogen on Neuronal Physiology. *Annual Review of Pharmacology and Toxicology* **47**, 657-680 (2007).
45. H. C. Lin *et al.*, NGN2 induces diverse neuron types from human pluripotency. *Stem Cell Reports* **16**, 2118-2127 (2021).
46. F. Zafra, D. Piniella, Proximity labeling methods for proteomic analysis of membrane proteins. *Journal of Proteomics* **264**, 104620 (2022).

47. L. Wang *et al.*, Analyses of the autism-associated neuroligin-3 R451C mutation in human neurons reveal a gain-of-function synaptic mechanism. *Molecular psychiatry*, (2022).
48. A. Pinggera *et al.*, New gain-of-function mutation shows CACNA1D as recurrently mutated gene in autism spectrum disorders and epilepsy. *Hum Mol Genet* **26**, 2923-2932 (2017).
49. M. B. Clark *et al.*, Long-read sequencing reveals the complex splicing profile of the psychiatric risk gene CACNA1C in human brain. *Molecular psychiatry* **25**, 37-47 (2020).
50. S. J. Sanders *et al.*, Progress in Understanding and Treating SCN2A-Mediated Disorders. *Trends in neurosciences* **41**, 442-456 (2018).
51. S. A. Sloan, J. Andersen, A. M. Pasca, F. Birey, S. P. Pasca, Generation and assembly of human brain region-specific three-dimensional cultures. *Nat Protoc*, (2018).
52. A. Nicolas *et al.*, Genome-wide Analyses Identify KIF5A as a Novel ALS Gene. *Neuron* **97**, 1268-1283 e1266 (2018).
53. A. Dobin *et al.*, STAR: ultrafast universal RNA-seq aligner. *Bioinformatics* **29**, 15-21 (2013).
54. Y. Liao, G. K. Smyth, W. Shi, featureCounts: an efficient general purpose program for assigning sequence reads to genomic features. *Bioinformatics* **30**, 923-930 (2014).
55. M. D. Robinson, D. J. McCarthy, G. K. Smyth, edgeR: a Bioconductor package for differential expression analysis of digital gene expression data. *Bioinformatics* **26**, 139-140 (2010).
56. G. E. Hoffman *et al.*, Transcriptional signatures of schizophrenia in hiPSC-derived NPCs and neurons are concordant with post-mortem adult brains. *Nat Commun* **8**, 2225 (2017).
57. A. M. Newman *et al.*, Determining cell type abundance and expression from bulk tissues with digital cytometry. *Nature biotechnology* **37**, 773-782 (2019).
58. G. E. Hoffman, E. E. Schadt, variancePartition: interpreting drivers of variation in complex gene expression studies. *BMC bioinformatics* **17**, 483 (2016).
59. M. E. Ritchie *et al.*, limma powers differential expression analyses for RNA-sequencing and microarray studies. *Nucleic Acids Res* **43**, e47 (2015).
60. N. L. Bray, H. Pimentel, P. Melsted, L. Pachter, Near-optimal probabilistic RNA-seq quantification. *Nature biotechnology* **34**, 525-527 (2016).
61. I. De Marinis, P. Lo Surdo, G. Cesareni, L. Perfetto, SIGNORApp: a Cytoscape 3 application to access SIGNOR data. *Bioinformatics* **38**, 1764-1766 (2022).
62. T. Stuart *et al.*, Comprehensive Integration of Single-Cell Data. *Cell* **177**, 1888-1902 e1821 (2019).

910 63. J. Urresti *et al.*, Correction: Cortical organoids model early brain development disrupted
911 by 16p11.2 copy number variants in autism. *Mol Psychiatry* **26**, 7581 (2021).
912 64. X. Yang *et al.*, Identification and validation of genes affecting aortic lesions in mice. *J Clin*
913 *Invest* **120**, 2414-2422 (2010).
914 65. K. Stefan, J. W. Harbour, SparK: A Publication-quality NGS Visualization Tool. *bioRxiv*,
915 845529 (2019).
916

Supplement for *Fernando et al., 2023*

		CONTROL				5'-DEL		3'-DEL		Genotype
										Data Point Color
Reference	Experiment	553-3	2607-4	3182-3	690-2	972-5	973-5	581-5	641-6	Donor Cell Line-Clone
Fig. 1 & Fig. S2	iGLUT/ iGABA generation	✓	✓	✓	✓	✓	✓	✓	✓	
	Immunostaining	✓	✓							
	Case/Control RNASeq	✓	✓			✓	✓	✓	✓	
Fig. 2 & Fig. S3	Case/Control MEA iGLUT	✓	✓			✓	✓	✓	✓	
	Case/Control MEA iGABA	✓	✓	✓	✓	✓	✓	✓	✓	
	Patch-Clamp iGLUT (Excitability)	✓	✓			✓	✓	✓	✓	
	Patch-Clamp iGABA (Excitability)	✓	✓			✓	✓	✓	✓	
Fig. S4	KCC2 MEA (GABAZine)			✓	✓					
Fig. 3	Patch-Clamp iGLUT (Neurotransmitter release)	✓	✓	✓	✓	✓	✓	✓	✓	
Fig. 3	Patch-Clamp iGABA (Neurotransmitter release)	✓	✓			✓	✓	✓	✓	
Fig. S5	TTX Experiments iGLUT	✓	✓			✓	✓	✓	✓	
Fig. S5	TTX Experiments iGABA	✓	✓		✓	✓	✓	✓	✓	
Fig. 4, Fig. S6 & S7	Organoid generation	✓	✓			✓	✓	✓	✓	
	Organoid characterization	✓	✓			✓	✓	✓	✓	
	Organoid rosette imaging	✓	✓			✓	✓	✓	✓	
	Organoid single cell sequencing	✓*	✓			✓	✓	✓	✓	
Fig. 5 & Fig S8.	shRNA testing iGLUT-WT	✓	✓	✓	✓					
	shRNA patch-clamp iGLUT-WT				✓					
	shRNA testing iGABA-WT	✓	✓	✓	✓					
	shRNA patch-clamp iGABA-WT		✓	✓	✓					
	shRNA testing iGLUT-MT							✓	✓	
	shRNA patch-clamp iGLUT-MT							✓		
	shRNA testing iGABA-MT							✓	✓	
	shRNA patch-clamp iGABA-MT							✓		
Fig. 5	Beta-Estradiol					✓	✓			
Fig. 5	Anti-sense Oligos							✓	✓	

Extended Data Figure 1: *Specific cell lines used in each experiment throughout this study.* Reference table of all cell lines-clones used per experiment with corresponding data point colors. Check marks indicate inclusion for experiments, *represents dropped donor due to failed QC.

a

	iGLUT 5'-Del		iGLUT 3'-Del		iGABA 5'-Del		iGABA 3'-Del	
	Overlapped DEGs with risk genes	Overlapped DEGs with risk genes & in SIGNOR database	Overlapped DEGs with risk genes	Overlapped DEGs with risk genes & in SIGNOR database	Overlapped DEGs with risk genes	Overlapped DEGs with risk genes & in SIGNOR database	Overlapped DEGs with risk genes	Overlapped DEGs with risk genes & in SIGNOR database
ASD	11	**7**	4	**0**	3	**1**	6	**2**
BP	16	**9**	3	**1**	2	**1**	5	**1**
SCZ	26	**14**	10	**1**	9	**3**	14	**3**
Total	37	**22**	12	**2**	9	**3**	18	**4**

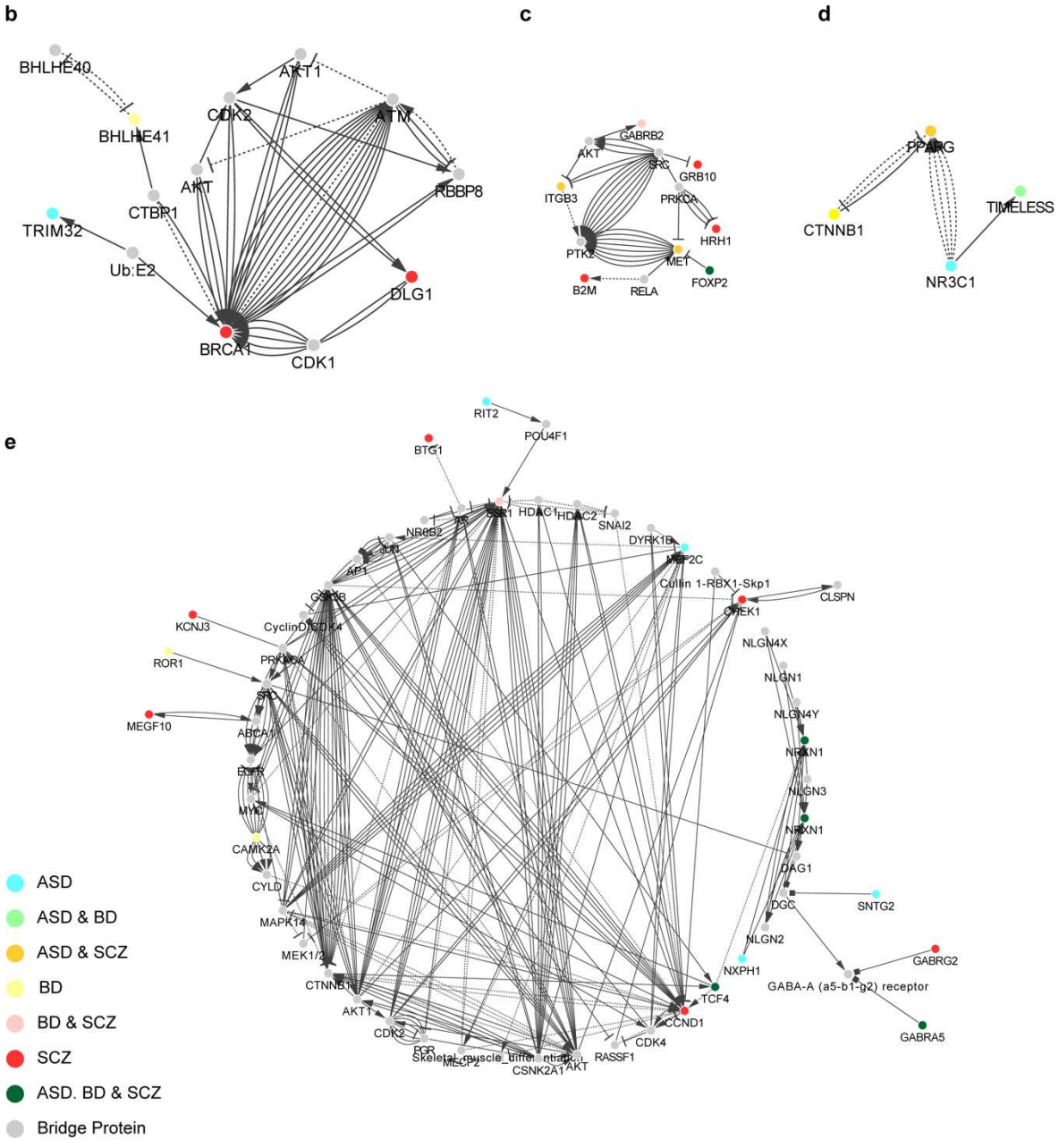

Extended Data Figure 2: *Extended transcriptomics analysis on disease risk associated genes.* (a) Summary table of overlapping DEGs with risk enrichments across publicly curated datasets for autism (ASD), bipolar disorder (BD) and schizophrenia. Interaction maps of risk genes for (b) 3'-Del iGLUT, (c) 3'-Del iGABA, (d) 5'-Del iGABA and (e) 5'-iGLUT. Sample information correspond to Fig. 1

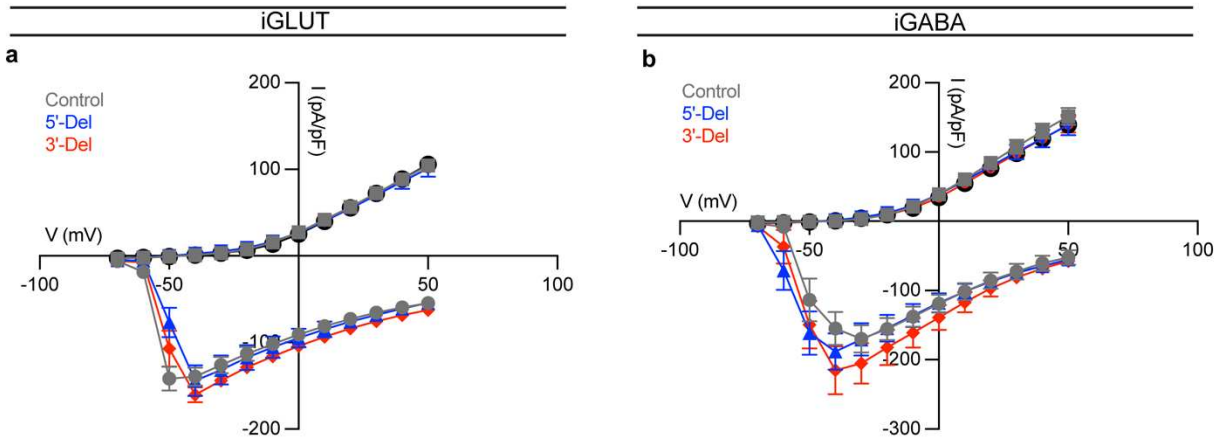

Extended Data Figure 3: *Extended data excitable properties of 5'-Del and 3'-Del neurons.* Voltage-gated potassium and channel kinetics across genotypes for (a) iGLUT (n = 6 donors | 2 inductions | 45 neurons) and (b) iGABA neurons (n = 6 donors | 2 inductions | 34 neurons).

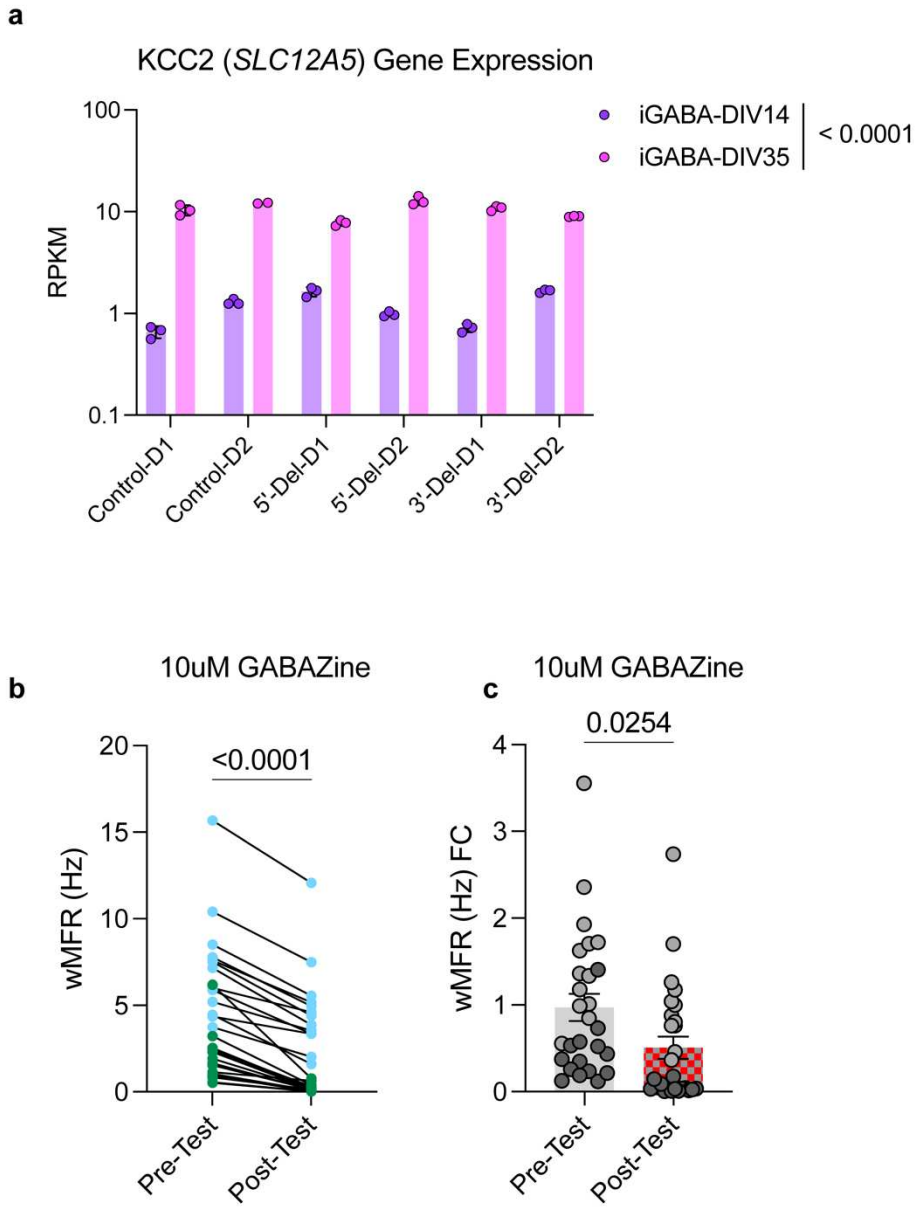

Extended Data Figure 4: *Extended KCC2 related data from immature GABA neurons.* (a) Transcriptomic comparison of *SLC12A5* expression across DIV14 and DIV35 RNASeq timepoints. (b,c) MEA tests from pre- and post- treatment of 10uM GABAzine. (n = 2 donors | 1 representative induction | 28 MEA wells) Statistical tests are paired student's t-test for time-linked comparison and unpaired student's t-test for pre/post activity foldchange.

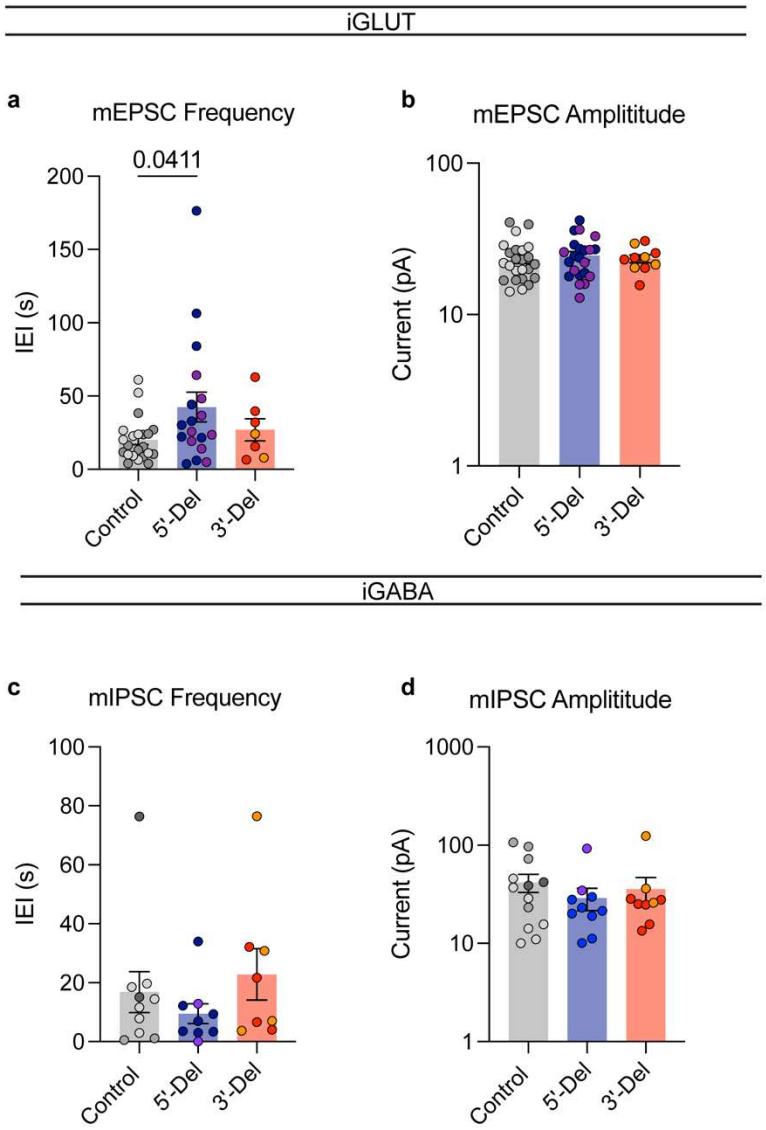

Extended Data Figure 5: *Miniature neurotransmitter release data (+TTX) from iGLUT and iGABA neurons.* Comparative mEPSC kinetics of (a) IEI and (b) amplitude size from iGLUT neurons (n= 6 donors | 4 inductions | 47 neurons). Statistical test used was a 1-way ANOVA with Dunnett's test. Comparative mIPSC kinetics of (a) IEI and (b) amplitude size from iGABA neurons (n= 6 donors | 3 inductions | 27 neurons). Statistical test used was a 1-way ANOVA with Dunnett's test.

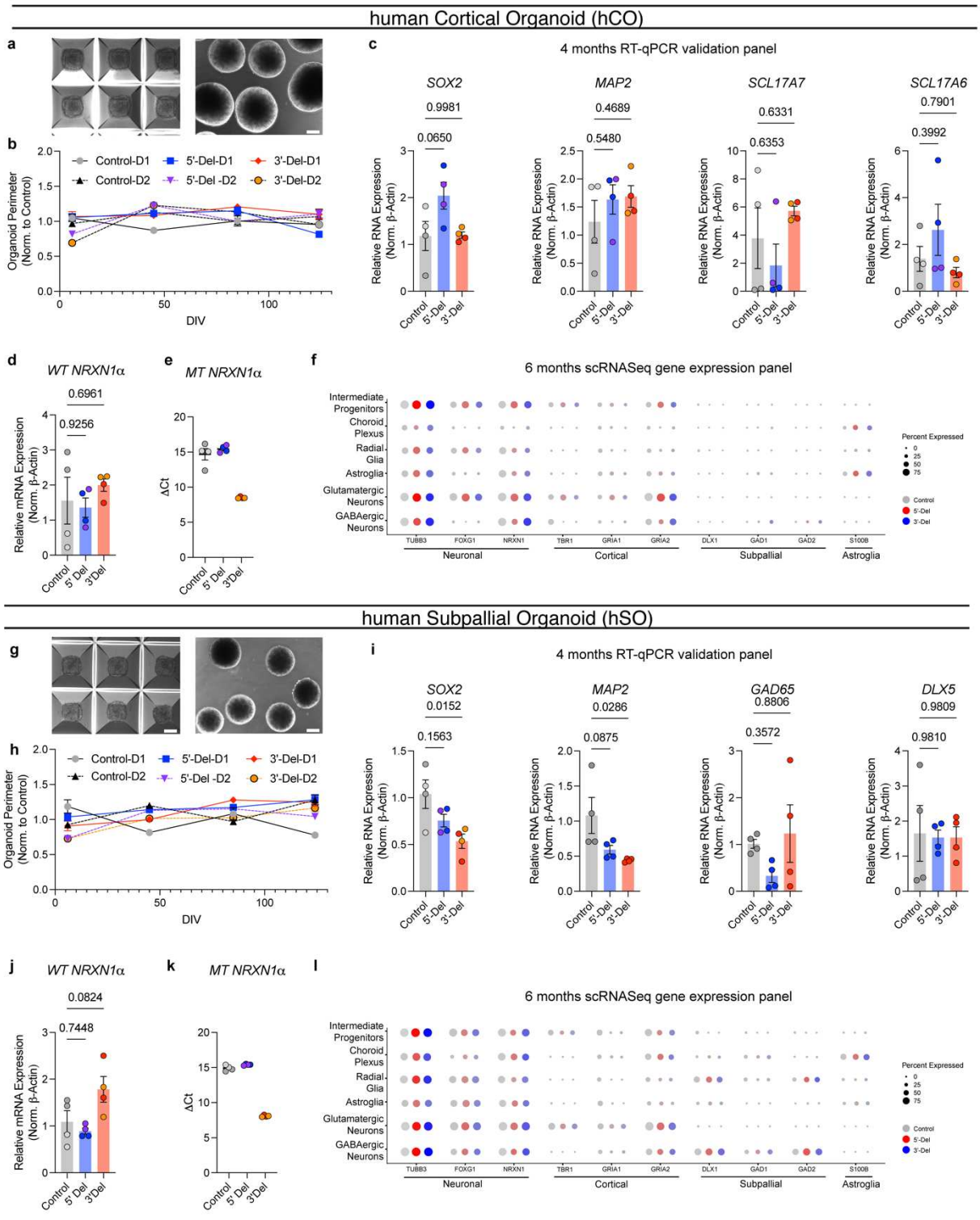

Extended Data Figure 6: *Extended data on human organoid generation and characterization.* (a,g) Representative images of hiPSC aggregation and immature spheroids post dislodging. (b,h) Normalized organoid perimeters over time (compared to averaged control), hCO (n = 6 donors | 2 batches | 72-161 organoids) and hSO (n = 6 donors | 2 batches | 46-134 organoids). (c, i) RT-qPCR results from 4-month organoids of genes for pluripotency, neuronal, and cell-type specific markers. (d-e, j-k) RT-qPCR results of *NRXN1* WT and MT expression hCO (n = 6 donors | 1 representative batch | 12 samples) and hSO (n = 6 donors | 1 representative batch | 12 samples). Statistical tests used were 1-way ANOVAs with Dunnett's test. (f, l) Comprehensive gene expression panel across sub-clusters of hCO and hSO samples across neuronal, cortical, subpallial and astroglia markers. Data corresponds to Fig 4.

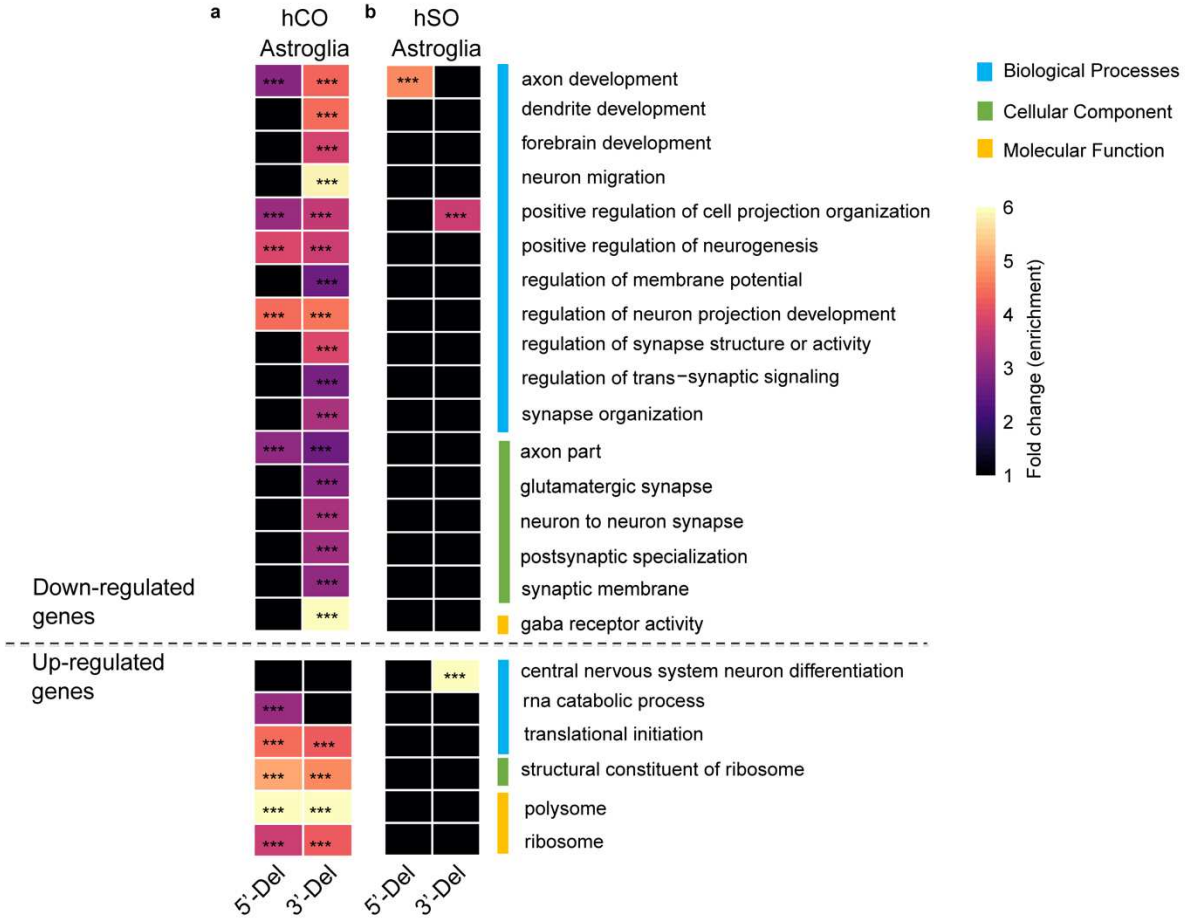

Extended Data Figure 7: *Extended analysis on astroglia subclusters from hCO and hSOs.* (a) hCO subcluster and (b) hCO subcluster GO analysis of overlapped terms with hCO-glutamatergic and hSO-GABAergic enrichments. *P < 0.05, **P < 0.01, ***P <0.001, Wilcoxon's rank sum test, FDR = 0.05.

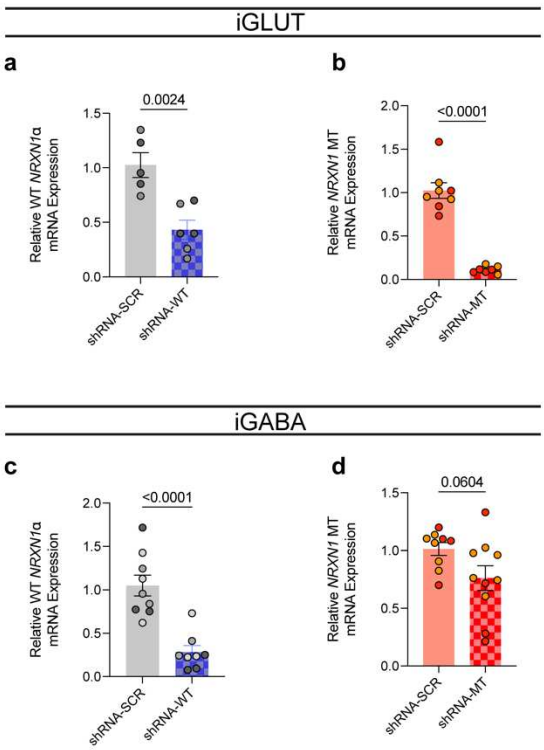

Extended Data Figure 8: *shRNA knockdown validation.* (a) Extent of shRNA knockdown on WT and (b) MT *NRXN1* expression in iGLUT neurons (n = 2 donors | 1-3 inductions). (c) Extent of shRNA knockdown on WT and (d) MT *NRXN1* expression in iGABA neurons, (n = 2-3 donors | 1-3 inductions) Statistical tests used were Student's t-test.

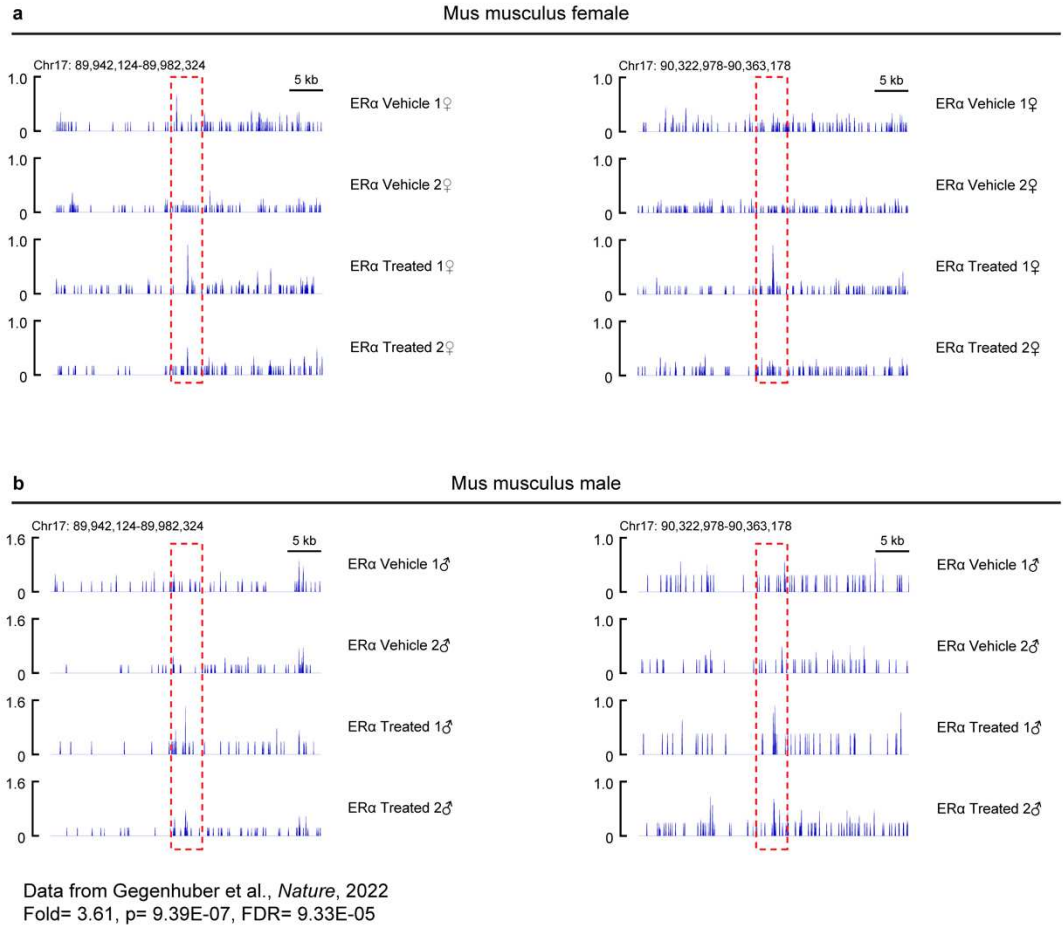

Extended Data Figure 9: *ChIP-seq enrichment of ER1 binding at NRXN1 loci in rodent brain.* (a) Female and (b) male mus musculus ChIP tracts of *NRXN1* locus, with red dashed areas highlighting binding enrichment across vehicle and estradiol treated mice.